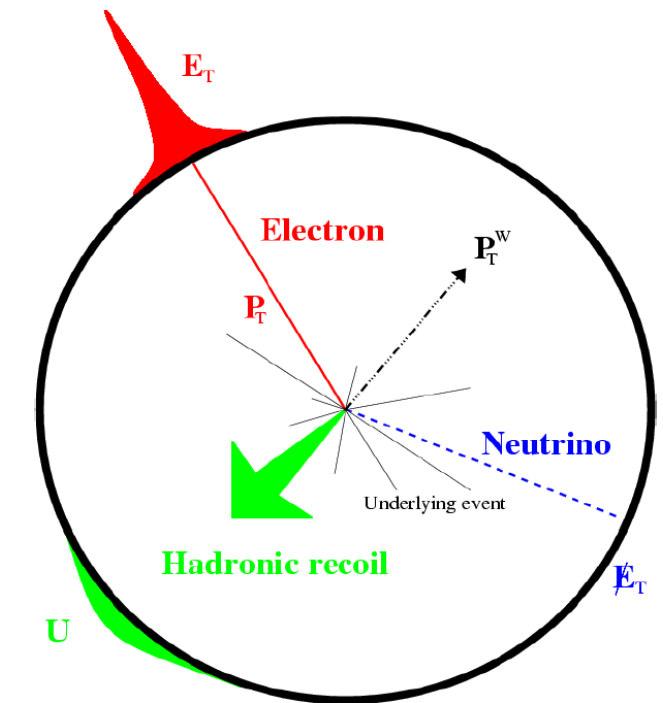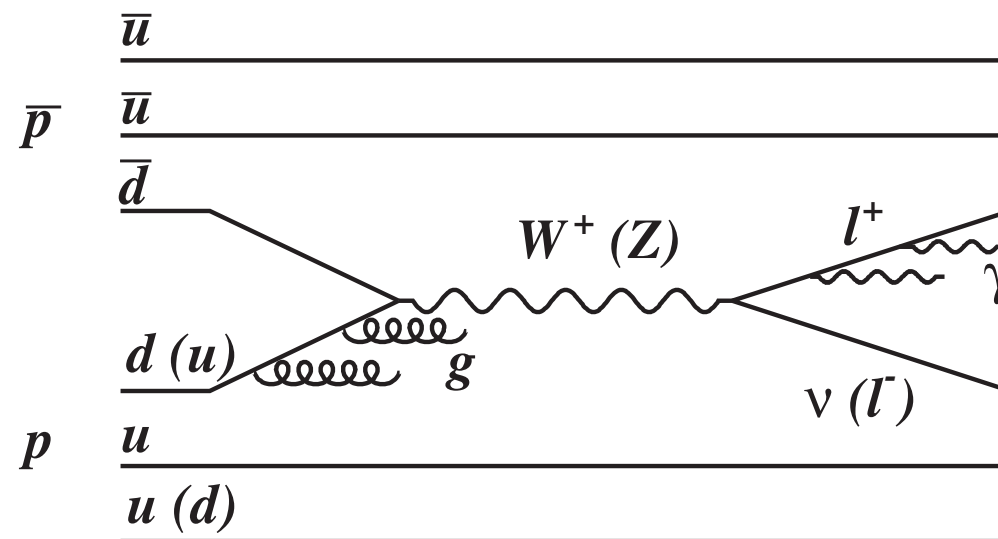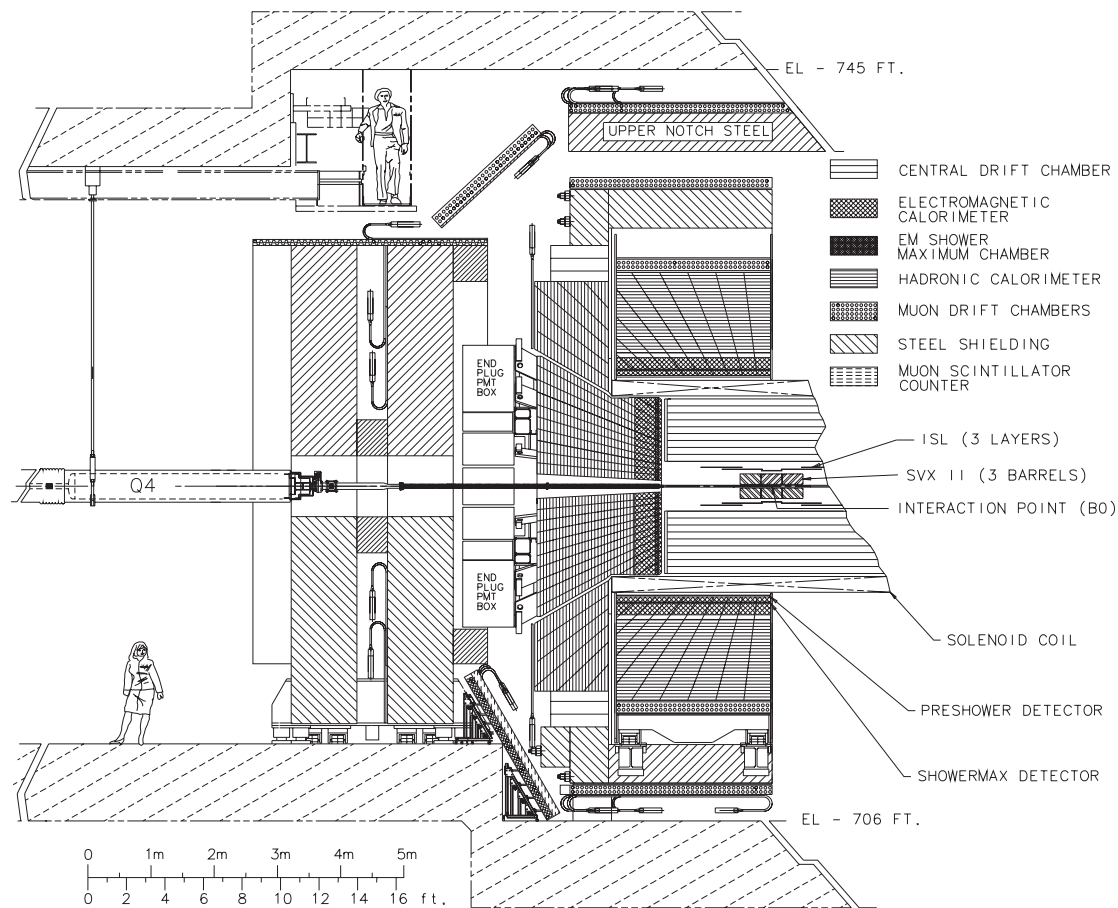# New m_W from CDF II (2022)

Youngjoon Kwon (Yonsei U.)
Workshop on m_W @ UoS, May 19, 2022

CDF W boson mass measurement
toward a new era in particle physics

A. V. Kotwal, SLAC, 4/11/22

2022/05/19 Centennial Memorial Bldg., NSRI, University of Seoul

PARTICLE PHYSICS

High-precision measurement of the *W* boson mass with the CDF II detector

CDF Collaboration†‡, T. Aaltonen[1,2], S. Amerio[3,4], D. Amidei[5], A. Anastassov[6], A. Annovi[7], J. Antos[8,9], G. Apollinari[6], J. A. Appel[6], T. Arisawa[10], A. Artikov[11], J. Asaadi[12], W. Ashmanskas[6], B. Auerbach[13], A. Aurisano[12], F. Azfar[14], W. Badgett[6], T. Bae[15,16,17,18,19,20,21], A. Barbaro-Galtieri[22], V. E. Barnes[23], B. A. Barnett[24], P. Barria[25,26], P. Bartos[8,9], M. Bauce[3,4], F. Bedeschi[25], S. Behari[6], G. Bellettini[25,27], J. Bellinger[28], D. Benjamin[29], A. Beretvas[6], A. Bhatti[30], K. R. Bland[31], B. Blumenfeld[24], A. Bocci[29], A. Bodek[32], D. Bortoletto[23], J. Boudreau[33], A. Boveia[34], L. Brigliadori[35,36], C. Bromberg[37], E. Brucken[1,2], J. Budagov[11]§, H. S. Budd[32], K. Burkett[6], G. Busetto[3,4], P. Bussey[38], P. Butti[25,27], A. Buzatu[38], A. Calamba[39], S. Camarda[40], M. Campanelli[41], B. Carls[42], D. Carlsmith[28], R. Carosi[25], S. Carrillo[43]§, B. Casal[44], M. Casarsa[45], A. Castro[35,36], P. Catastini[46], D. Cauz[45,47,48], V. Cavaliere[42], A. Cerri[22], L. Cerrito[41], Y. C. Chen[49], M. Chertok[50], G. Chiarelli[25], G. Chlachidze[6], K. Cho[15,16,17,18,19,20,21], D. Chokheli[11], A. Clark[51], C. Clarke[52], M. E. Convery[6], J. Conway[50], M. Corbo[6], M. Cordelli[7], C. A. Cox[50], D. J. Cox[50], M. Cremonesi[25], D. Cruz[12], J. Cuevas[44], R. Culbertson[6], N. d'Ascenzo[6], M. Datta[6], P. de Barbaro[32], L. Demortier[30], M. Deninno[35]§, M. D'Errico[3,4], F. Devoto[1,2], A. Di Canto[25,27], B. Di Ruzza[6], J. R. Dittmann[31], S. Donati[25,27], M. D'Onofrio[53], M. Dorigo[45,54], A. Driutti[45,47,48], K. Ebina[10], R. Edgar[5], A. Elagin[34], R. Erbacher[50], S. Errede[42], B. Esham[42], S. Farrington[14], J. P. Fernández Ramos[55], R. Field[43], G. Flanagan[6], R. Forrest[50], M. Franklin[46], J. C. Freeman[6], H. Frisch[34], Y. Funakoshi[10], C. Galloni[25,27], A. F. Garfinkel[23], P. Garosi[25,26], H. Gerberich[42], E. Gerchtein[6], S. Giagu[56], V. Giakoumopoulou[57], K. Gibson[33], C. M. Ginsburg[6], N. Giokaris[57]§, P. Giromini[7], V. Glagolev[11], D. Glenzinski[6], M. Gold[58], D. Goldin[12], A. Golossanov[6], G. Gomez[44], G. Gomez-Ceballos[59], M. Goncharov[59], O. González López[55], I. Gorelov[58], A. T. Goshaw[29], K. Goulianos[30], E. Gramellini[35], C. Grosso-Pilcher[34], J. Guimaraes da Costa[46], S. R. Hahn[6], J. Y. Han[32], F. Happacher[7], K. Hara[60], M. Hare[61], R. F. Harr[52], T. Harrington-Taber[6], K. Hatakeyama[31], C. Hays[14], J. Heinrich[62], M. Herndon[28], A. Hocker[6], Z. Hong[12], W. Hopkins[6], S. Hou[49], R. E. Hughes[63], U. Husemann[64], M. Hussein[37], J. Huston[37], G. Introzzi[25,65,66], M. Iori[56,67], A. Ivanov[50], E. James[6], D. Jang[39], B. Jayatilaka[6], E. J. Jeon[15,16,17,18,19,20,21], S. Jindariani[6], M. Jones[23], K. K. Joo[15,16,17,18,19,20,21], S. Y. Jun[39], T. R. Junk[6], M. Kambeitz[68], T. Kamon[15,16,17,18,19,20,21,12], P. E. Karchin[52], A. Kasmi[31], Y. Kato[69], W. Ketchum[34], J. Keung[62], B. Kilminster[6], D. H. Kim[15,16,17,18,19,20,21], H. S. Kim[6], J. E. Kim[15,16,17,18,19,20,21], M. J. Kim[7], S. H. Kim[60], S. B. Kim[15,16,17,18,19,20,21], Y. J. Kim[15,16,17,18,19,20,21], Y. K. Kim[34], N. Kimura[10], M. Kirby[6], K. Kondo[10]§, D. J. Kong[15,16,17,18,19,20,21], J. Konigsberg[43], A. V. Kotwal[29]*, M. Kreps[68], J. Kroll[62], M. Kruse[29], T. Kuhr[68], M. Kurata[60], A. T. Laasanen[23], S. Lammel[6], M. Lancaster[41], K. Lannon[63], G. Latino[25,26], H. S. Lee[15,16,17,18,19,20,21], J. S. Lee[15,16,17,18,19,20,21], S. Leo[42], S. Leone[25], J. D. Lewis[6], A. Limosani[29], E. Lipeles[62], A. Lister[51], Q. Liu[23], T. Liu[6], S. Lockwitz[64], A. Loginov[64]§, D. Lucchesi[3,4], A. Lucà[7,6], J. Lueck[68], P. Lujan[22], P. Lukens[6], G. Lungu[30], J. Lys[22]§, R. Lysak[8,9], R. Madrak[6], P. Maestro[25,26], S. Malik[30], G. Manca[53], A. Manousakis-Katsikakis[57], L. Marchese[35], F. Margaroli[56], P. Marino[25,70], K. Matera[42], M. E. Mattson[52], A. Mazzacane[6], P. Mazzanti[35], R. McNulty[53], A. Mehta[53], P. Mehtala[1,2], A. Menzione[25]§, C. Mesropian[30], T. Miao[6], E. Michielin[3,4], D. Mietlicki[5], A. Mitra[49], H. Miyake[60], S. Moed[6], N. Moggi[35]

Disclaimers

- I am not from CDF, nor have any expertise in hadron collisions.

- So, this presentation will be more like a journal club talk, rather than a full-blown seminar.

- Nevertheless, your active participation with questions/comments are welcome, and we can think together.

- This talk is based on the following documents:

  - CDF II paper : Science, 376, 170 (2022) with supplemental materials, for the new measurement

  - Seminar slides by Ashutosh Kotwal (Duke) presented at SLAC, Apr. 11, 2022

  - CDF paper : PRD 89, 072003 (2014), for the previous measurement
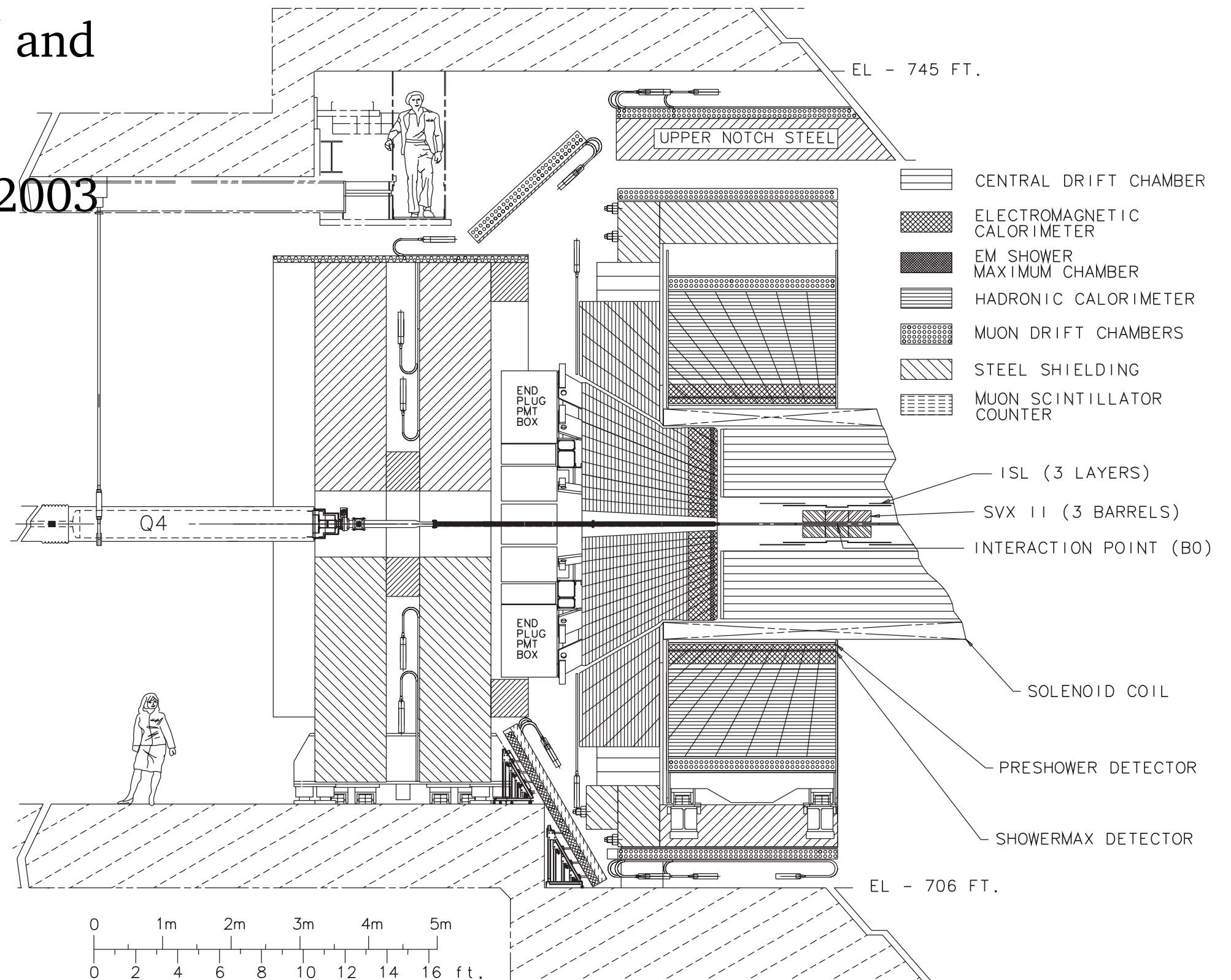
Science 376, 170 (2022)
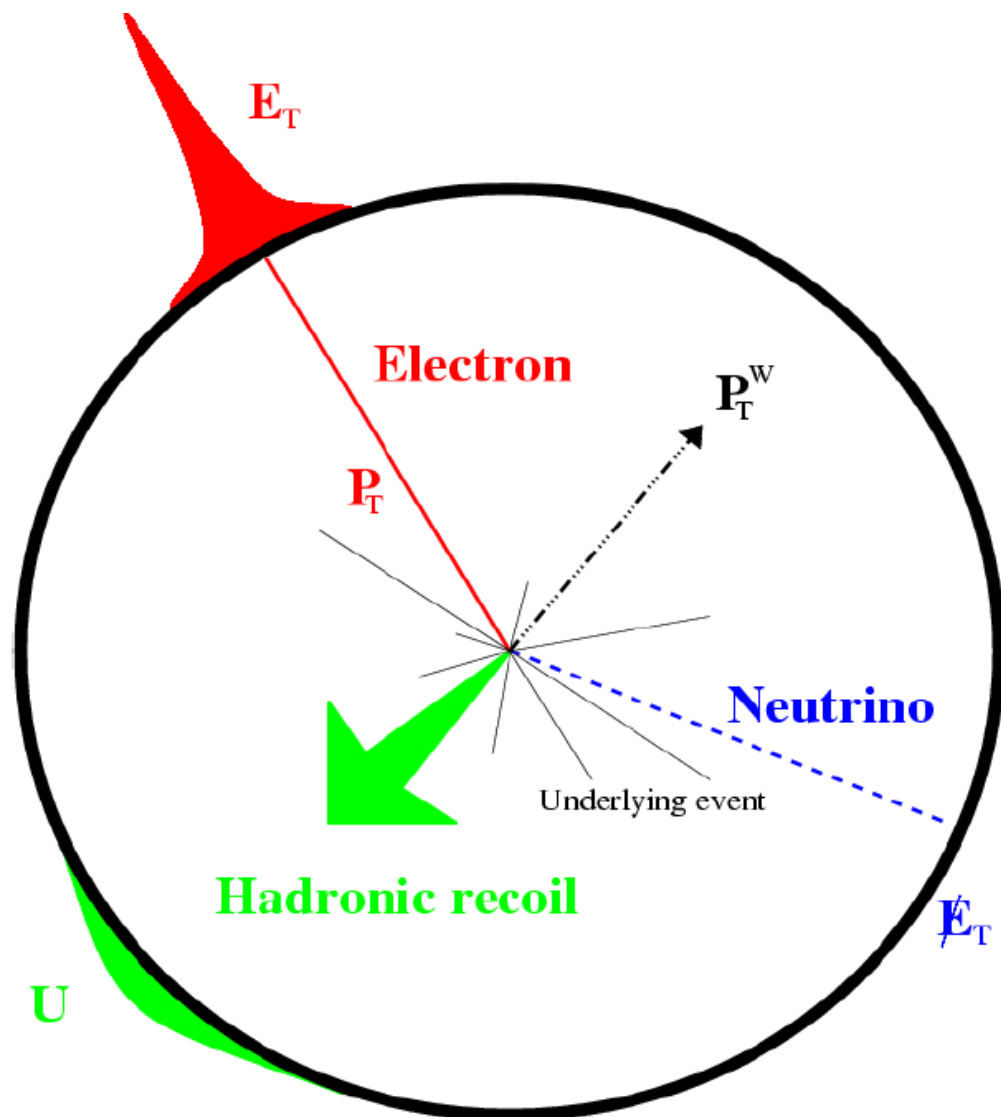
- Intro — m_W in SM and beyond

- CDF experiment

- W, Z event selection

- Simulation of signal processes

- Calibration of $\vec{p}$, E

- Extracting m_W

- Discussions

$p\bar{p}$ vs. pp

$p\bar{p}$ (CDF, DØ)

pp (CMS, ATLAS)
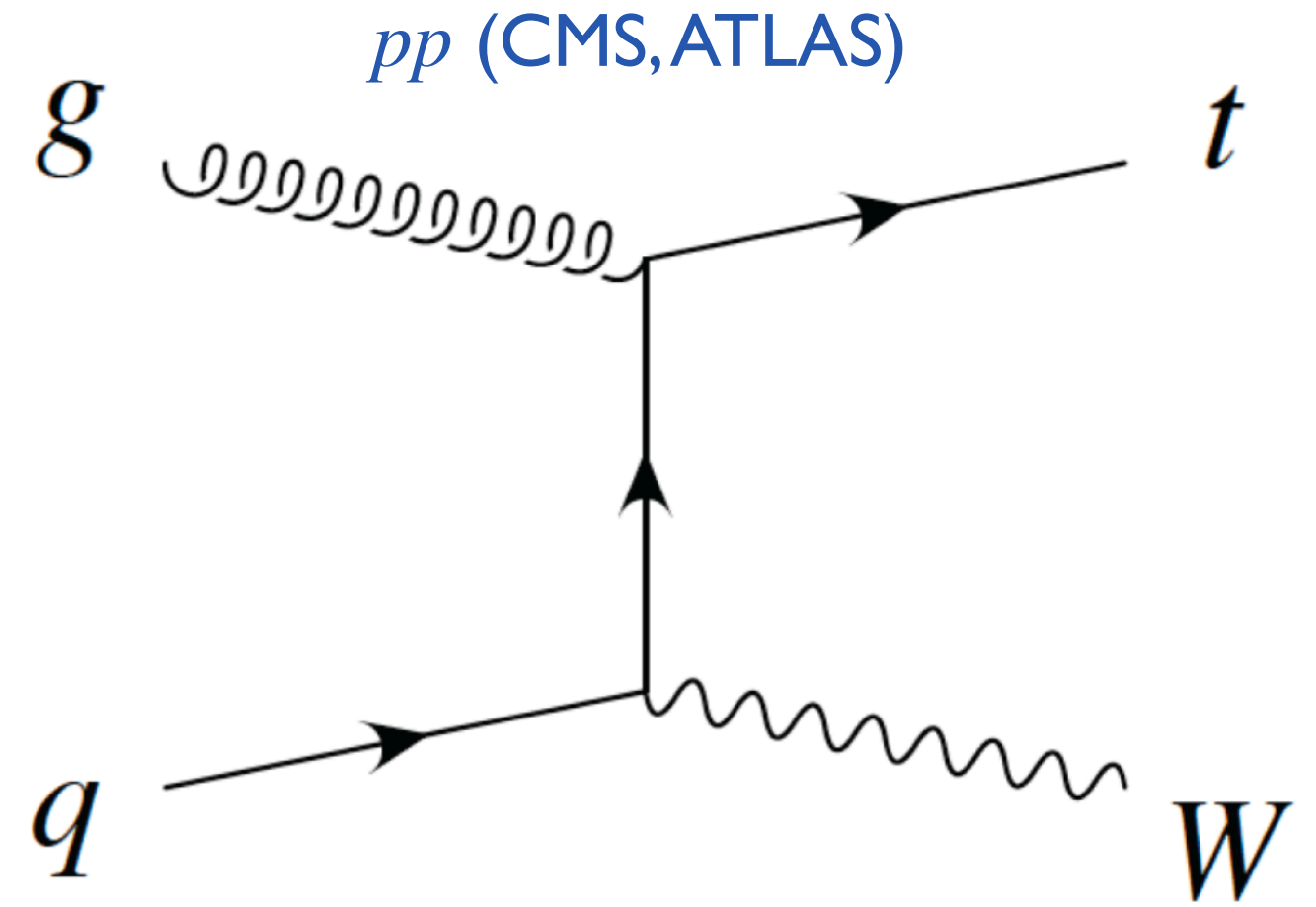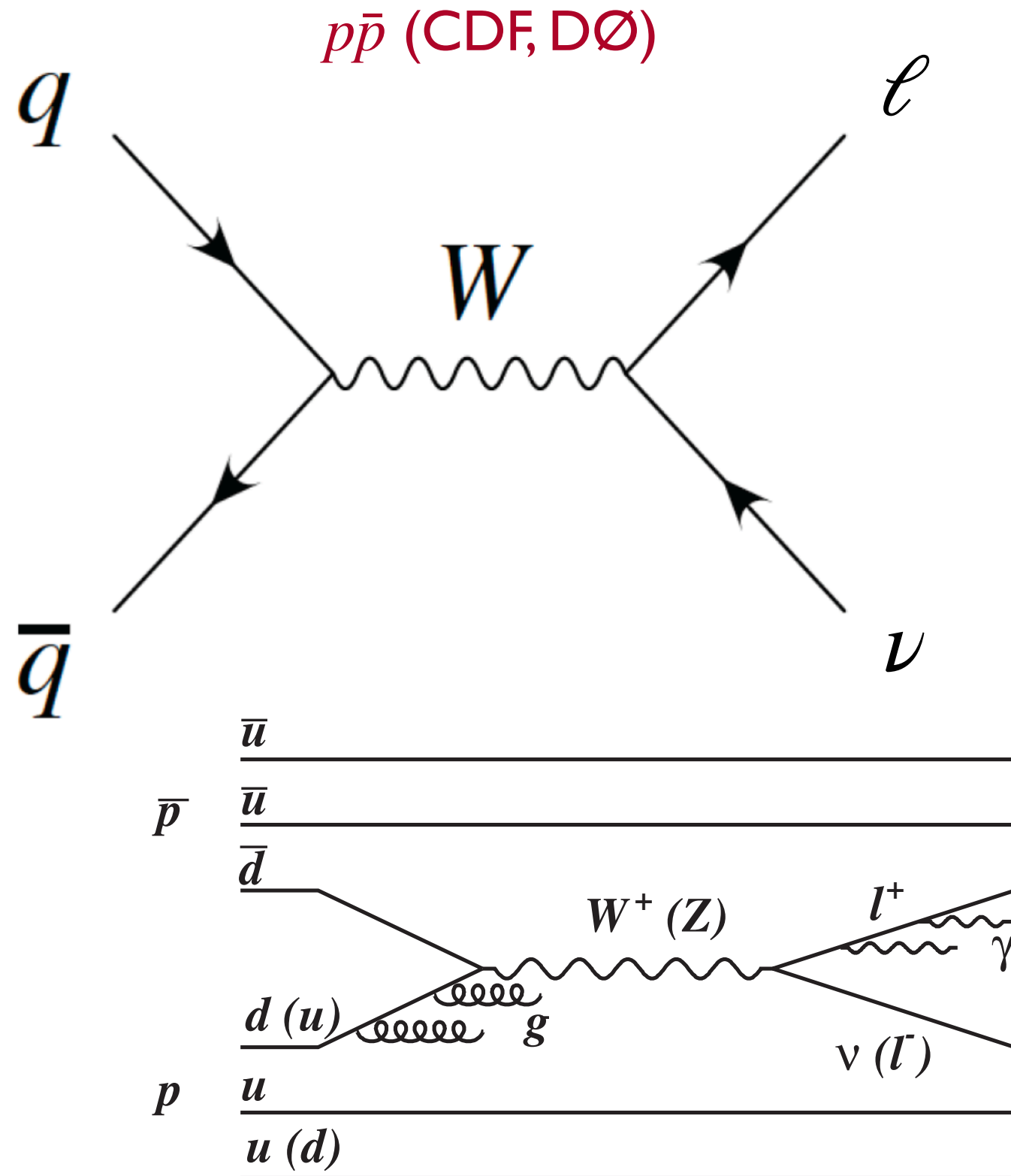
The CDF II experiment

- $p\bar{p}$ collision with $\sqrt{s} = 1.96$ TeV and $\mathscr{L}_{\text{int}} = 8.8$ fb^{-1}

- previous m_W result in PRD 89, 072003 (2014) w/ $\mathscr{L}_{\text{int}} = 2.2$ fb^{-1}

W, Z **event selection**

W and Z boson event selection

Events with a candidate muon with $p_T > 18$ GeV or electron with $E_T > 18$ GeV (50) are selected online by the trigger system for offline analysis. The following offline criteria select fairly pure samples of $W \to \mu\nu$ and $W \to e\nu$ decays. Muon candidates must have $p_T > 30$ GeV, with requirements on COT-track quality, calorimeter-energy depo-

sition, and muon-chamber signals. Cosmic-ray muons are rejected with a targeted tracking algorithm (51). Electron candidates must have a COT track with $p_T > 18$ GeV and an EM calorimeter-energy deposition with $E_T > 30$ GeV and must meet requirements for COT track quality, matching of position and energy measured in the COT and in the calorimeter ($E_T/p_T < 1.6$), and spatial distributions of energy depositions in the calorimeters (43). Leptons are required to be central in pseudorapidity ($|\eta| < 1$) (50) and within the fiducial region where the relevant detector systems have high efficiency and uniform response. When selecting the W boson candidate sample, we suppress the Z boson background by rejecting events with a second lepton of the same flavor. Events that contain two oppositely charged leptons of the same flavor with invariant mass in the range of 66 to 116 GeV and with dilepton $p_T < 30$ GeV provide Z boson control samples ($Z \to ee$ and $Z \to \mu\mu$) to measure the detector response, resolution, and efficiency, as well as the boson p_T distributions. Details of the event selection criteria are described in (43).

The W boson mass is inferred from the

containing energy deposition from the charged lepton(s) are excluded from this sum. The transverse momentum vector of the neutrino $\vec{p}_T^{\,\nu}$ is inferred as $\vec{p}_T^{\,\nu} \equiv -\vec{p}_T^{\,\ell} - \vec{u}$ from $\vec{p}_T$ conservation, where $\vec{p}_T^{\,\ell}$ is the vector p_T (E_T) of the muon (electron). In analogy with a two-body mass, the W boson transverse mass is defined using only the transverse momentum vectors as $m_T = \sqrt{2\left(p_T^\ell p_T^\nu - \vec{p}_T^{\,\ell} \cdot \vec{p}_T^{\,\nu}\right)}$ (53).

High-purity samples of W bosons are obtained with the requirements $30 < p_T^\ell < 55$ GeV, $30 < p_T^\nu < 55$ GeV, $|\vec{u}| < 15$ GeV, and $60 < m_T < 100$ GeV. This selection retains samples containing precise M_W information and low backgrounds. The final samples of W and Z bosons consist of 1,811,700 (66,180) $W \to e\nu$ ($Z \to ee$) candidates and 2,424,486 (238,534) $W \to \mu\nu$ ($Z \to \mu\mu$) candidates.

Simulation of physical processes

The data distributions of m_T, p_T^ℓ, and p_T^ν are compared with corresponding simulated line shapes ("templates") as functions of M_W from a custom Monte Carlo simulation that has been
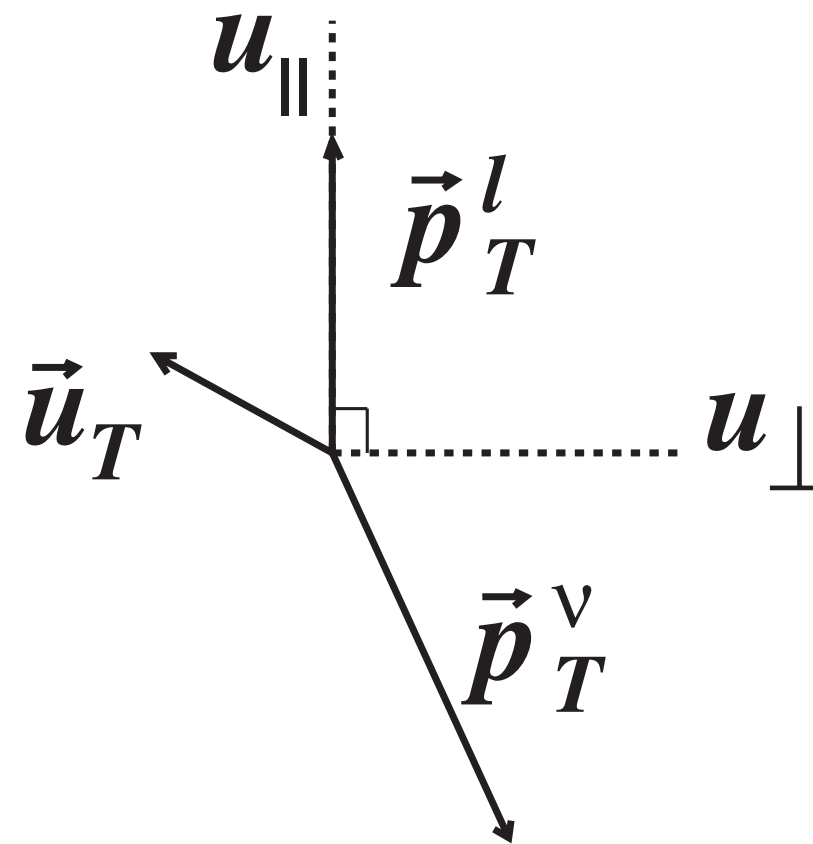
W, Z **event selection**

$p_T < 30$ GeV provide Z boson control samples ($Z \rightarrow ee$ and $Z \rightarrow \mu\mu$) response, resolution, the boson p_T distribu... selection criteria are described in (43).

The W boson mass is inferred from the kinematic distributions of the decay leptons (ℓ). Because the neutrino from the W boson decay is not directly detectable, its transverse momentum p_T^ν is deduced by imposing transverse momentum conservation. Longitudinal momentum balance cannot be imposed because most of the beam momenta are carried away by collision products that remain close to the beam axis, outside the instrumented regions of the detector. By design of the detector, such products have small transverse momentum. The transverse momentum vector sum of all detectable collision products accompanying the W or Z boson is defined as the hadronic recoil $\vec{u} = \Sigma_i E_i \sin(\theta_i)\hat{n}_i$, where the sum is performed over calorimeter towers (52) with energy E_i, polar angle θ_i, and transverse directions specified by unit vectors $\hat{n}_i$. Calorimeter towers

shapes ("templates") as functions of M_W from a custom Monte Carlo simulation that has been de... A binned lik... mass and its... ic proper- tie... decay are si... (54–56), wh... ss section wi... momen- tu... tion and de... at next- to... quantum ch... next-to- ne... ation of higher-order radiative quantum amplitudes. RESBOS offers one of the most accurate theoretical calculations available for these processes. The nonperturbative model parameters in RESBOS and the QCD interaction coupling strength α_s are external inputs needed to complete the description of the boson p_T spectrum and
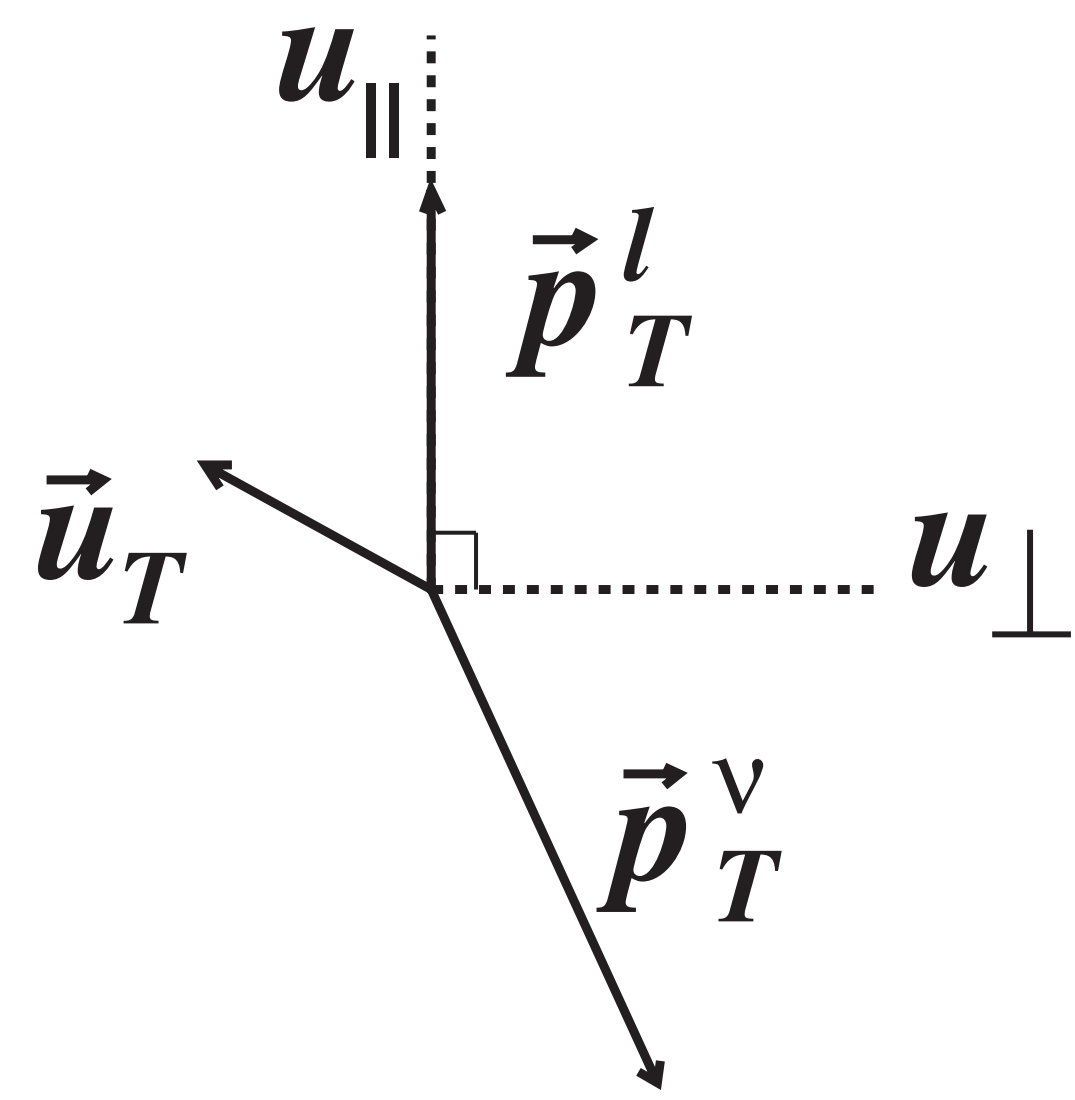
containing energy (
lepton(s) are excl
transverse mome

trino $\vec{p}_T^{\,\nu}$ is inferred as $\vec{p}_T^{\,\nu} \equiv -\vec{p}_T^{\,\ell} - \vec{u}$ from $\vec{p}_T$ conservation, where $\vec{p}_T^{\,\ell}$ is the vector p_T (E_T) of the muon (electron). In analogy with a two-body mass, the W boson transverse mass is defined using only the transverse momentum vectors as $m_T = \sqrt{2\left(p_T^\ell p_T^\nu - \vec{p}_T^{\,\ell} \cdot \vec{p}_T^{\,\nu}\right)}$ (53).

High-purity samples of W bosons are obtained with the requirements $30 < p_T^\ell < 55$ GeV, $30 < p_T^\nu < 55$ GeV, $|\vec{u}| < 15$ GeV, and $60 < m_T < 100$ GeV. This selection retains samples containing precise M_W information and low backgrounds. The final samples of W and Z bosons consist of 1,811,700 (66,180) $W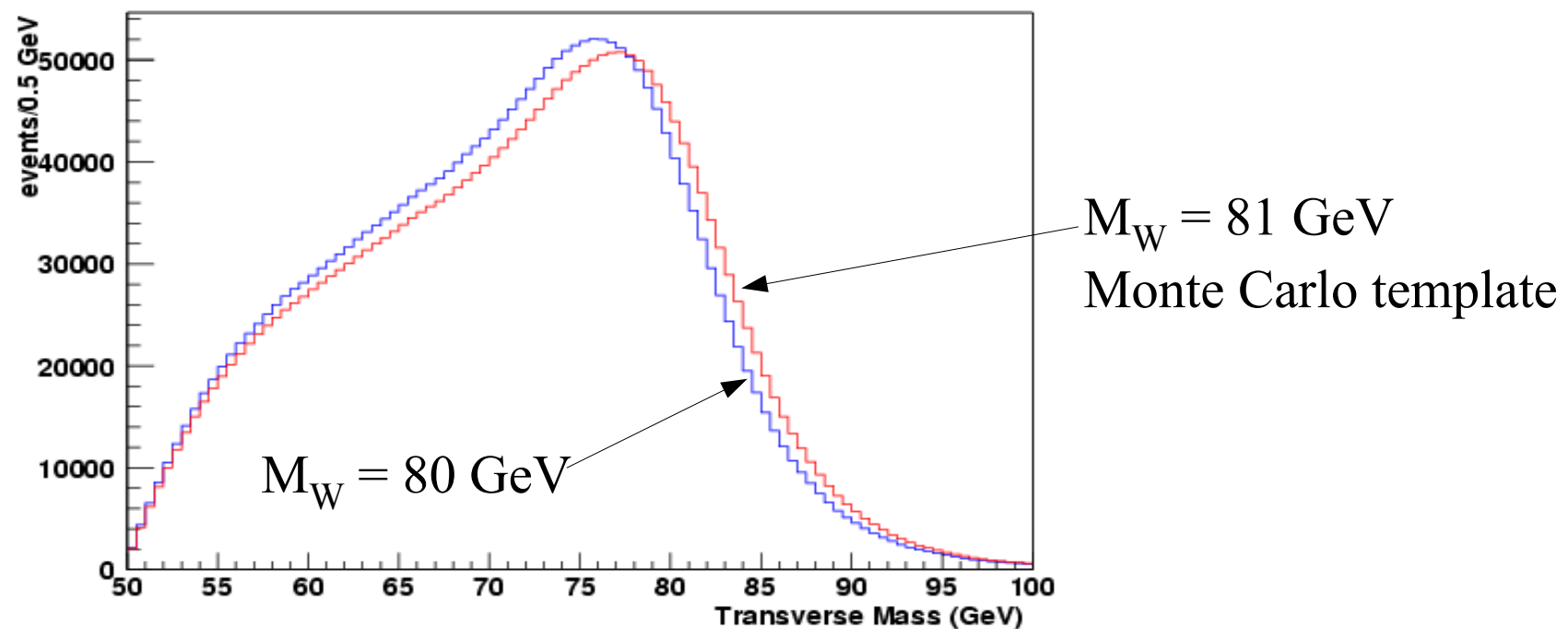 \rightarrow e\nu$ ($Z \rightarrow ee$) candidates and 2,424,486 (238,534) $W \rightarrow \mu\nu$ ($Z \rightarrow \mu\mu$) candidates.

Simulation of physical processes

The data distributions of m_T, p_T^ℓ, and p_T^ν are compared with corresponding simulated line

candidates and 2,424,486 (238,534) $W \to \mu\nu$ ($Z \to \mu\mu$) candidates.

Simulation of physical processes

The data distributions of m_T, p_T^ℓ, and p_T^ν are compared with corresponding simulated line shapes ("templates") as functions of M_W from a custom Monte Carlo simulation that has been designed and written for this analysis. A binned likelihood is maximized to obtain the mass and its statistical uncertainty. The kinematic properties of W and Z boson production and decay are simulated using the RESBOS program (54–56), which calculates the differential cross section with respect to boson mass, transverse momentum, and rapidity for boson production and decay. The calculation is performed at next-to-leading order in perturbative quantum chromodynamics (QCD), along with next-to-next-to-leading logarithm resummation of higher-order radiative quantum amplitudes. RESBOS offers one of the most accurate theoretical calculations available for these processes. The nonperturbative model parameters in RESBOS and the QCD interaction coupling strength α_s are external inputs needed to complete the description of the boson p_T spectrum and

Simulation of signals

- All signals simulated using a Custom Monte Carlo
  - Generate finely-spaced templates as a function of the fit variable
  - perform binned maximum-likelihood fits to the data
- Custom fast Monte Carlo makes smooth, high statistics templates
  - And provides analysis control over key components of the simulation
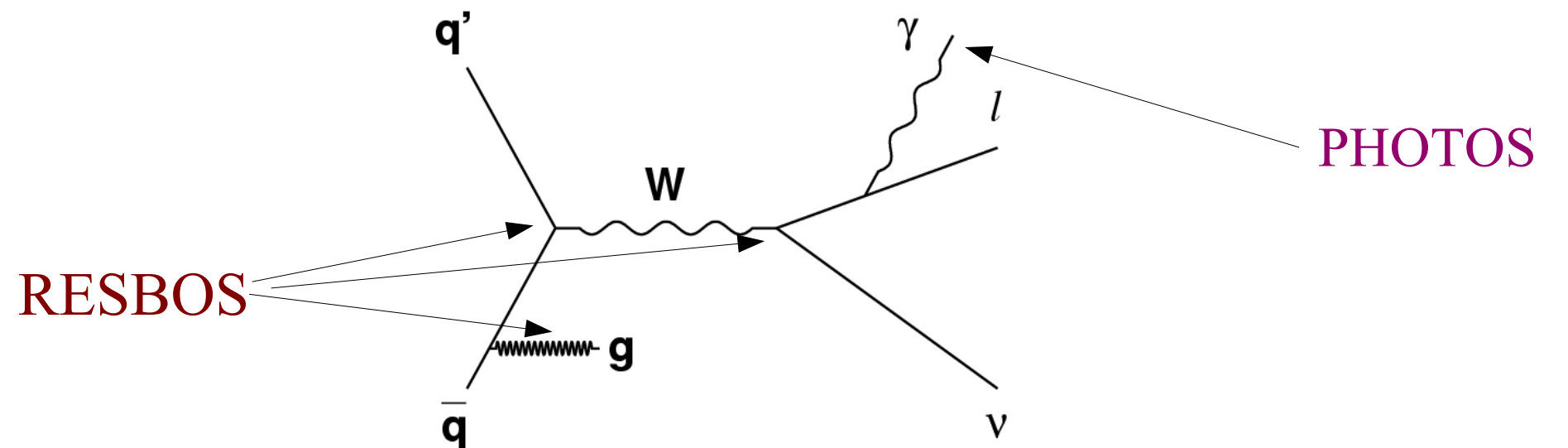

$M_W = 81$ GeV
Monte Carlo template

$M_W = 80$ GeV

- We will extract the W mass from six kinematic distributions: Transverse mass, charged lepton p_T and missing E_T using both electron and muon channels

A. V. Kotwal, SLAC, 4/11/22

Simulation of physical processes

Simulation of signals

The data distributions of m_T, p_T^ℓ, and p_T^ν are compared with corresponding simulated line shapes ("templates") as functions of M_W from a custom Monte Carlo simulation that has been designed and written for this analysis. A binned likelihood is maximized to obtain the mass and its statistical uncertainty. The kinematic properties of W and Z boson production and decay are simulated using the RESBOS program (*54–56*), which calculates the differential cross section with respect to boson mass, transverse momentum, and rapidity for boson production and decay. The calculation is performed at next-to-leading order in perturbative quantum chromodynamics (QCD), along with next-to-next-to-leading logarithm resummation of higher-order radiative quantum amplitudes. RESBOS offers one of the most accurate theoretical calculations available for these processes. The nonperturbative model parameters in RESBOS and the QCD interaction coupling strength α_S are external inputs needed to complete the description of the boson p_T spectrum and

- Generator-level input for W & Z simulation provided by RESBOS (C. Balazs & C.-P. Yuan, PRD56, 5558 (1997) and references therein), which

  – Calculates triple-differential production cross section, and p_T-dependent double-differential decay angular distribution

  – calculates boson p_T spectrum reliably over the relevant p_T range: includes tunable parameters in the non-perturbative regime at low p_T

- Multiple radiative photons generated according to PHOTOS (P. Golonka and Z. Was, Eur. J. Phys. C 45, 97 (2006) and references therein)

A. V. Kotwal, SLAC, 4/11/22

to-leading order in perturbative quantum chromodynamics (QCD) along with next-to-next-to-leading logarithm higher-order radiative q RESBOS offers one of the most accurate theoretical calculations available for these processes. The nonperturbative model parameters in RESBOS and the QCD interaction coupling strength α_s are external inputs needed to complete the description of the boson p_T spectrum and are constrained from the high-resolution dilepton $p_T^{\ell\ell}$ spectrum of the Z boson data and the p_T^W data spectrum. EM radiation from the leptons is modeled with the PHOTOS program (57), which is calibrated to the more accurate HORACE program (58, 59). We use the NNPDF3.1 (60) parton distribution functions (PDFs) of the (anti)proton, as they incorporate the most complete relevant datasets of the available next-to-next-to-leading order (NNLO) PDFs. Using 25 symmetric eigenvectors of the NNPDF3.1 set, we estimate a PDF uncertainty of 3.9 MeV. We find that the CT18 (61), MMHT2014 (62), and NNPDF3.1 NNLO PDF sets produce consistent results for the W boson
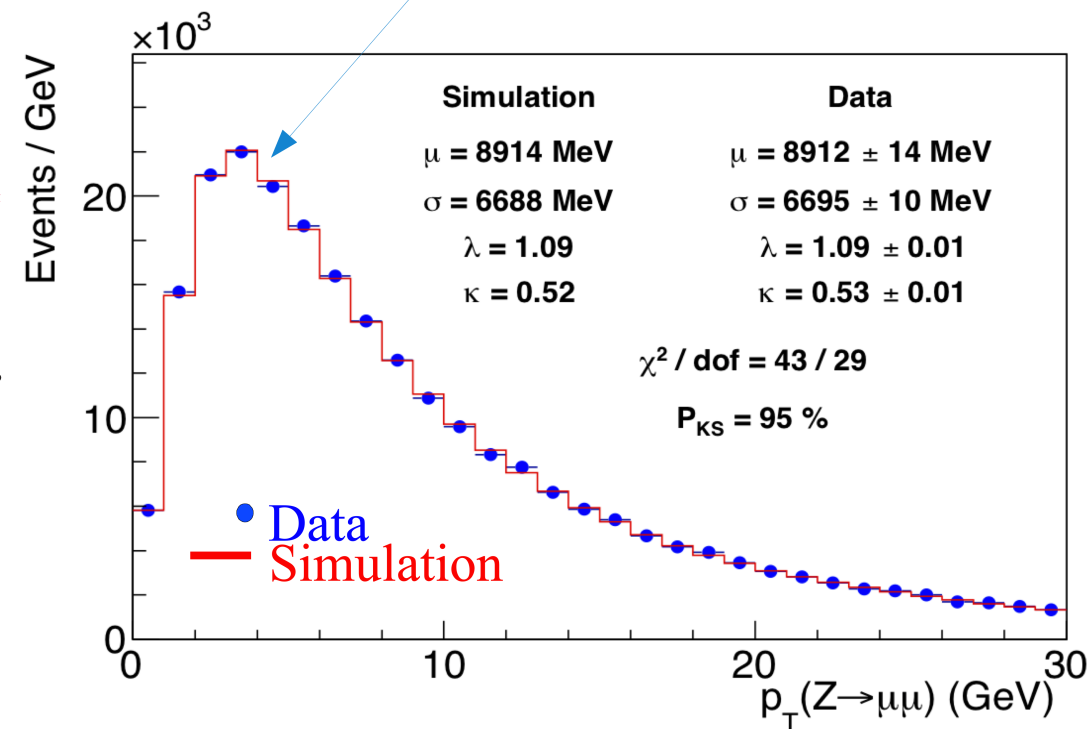
Simulation of signals

Constraining Boson p_T Spectrum

- Fit the non-perturbative parameter g_2 and QCD coupling α_S in RESBOS to $p_T(ll)$ spectra:

$$\Delta M_W = 1.8 \text{ MeV}$$

Position of peak in boson p_T spectrum depends on g_2
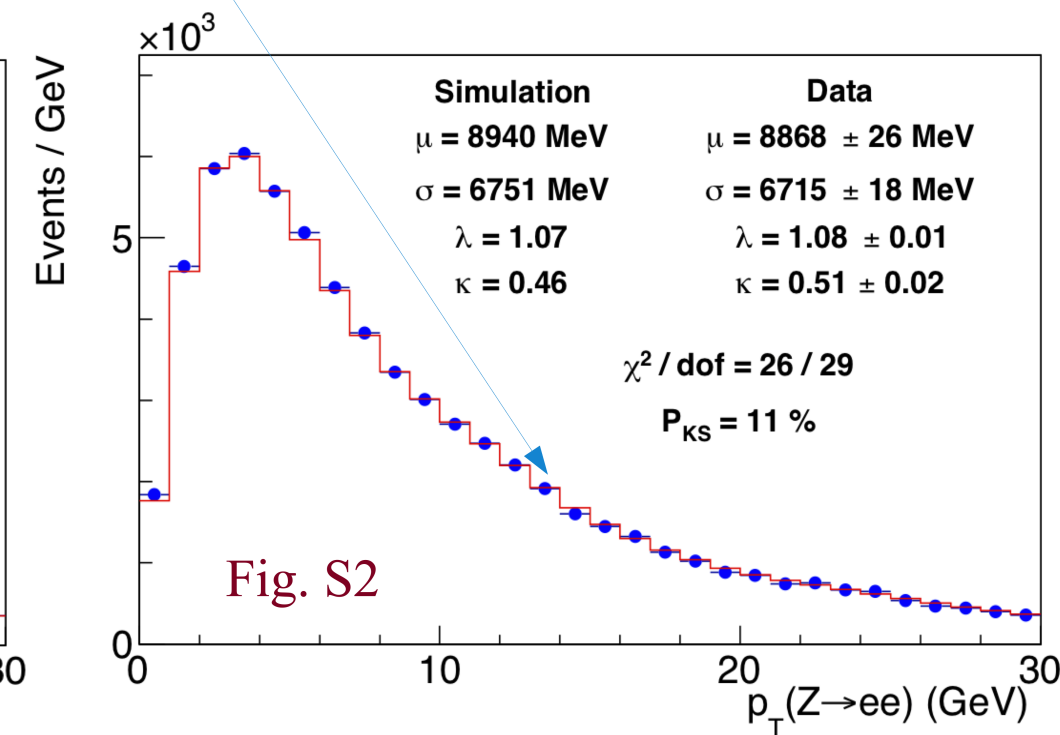
Tail to peak ratio depends on α_S

Fig. S2

A. V. Kotwal, SLAC, 4/11/22

Simulation of signals

RESBOS offers one of the most accurate theoretical calculations available for nonperturbative model parameters and the QCD interaction coupling strengths are external inputs needed to complete the description of the boson p_T spectrum and are constrained from the high-resolution dilepton $p_T^{\ell\ell}$ spectrum of the Z boson data and the p_T^W data spectrum. EM radiation from the leptons is modeled with the PHOTOS program (57), which is calibrated to the more accurate HORACE program (58, 59). We use the NNPDF3.1 (60) parton distribution functions (PDFs) of the (anti)proton, as they incorporate the most complete relevant datasets of the available next-to-next-to-leading order (NNLO) PDFs. Using 25 symmetric eigenvectors of the NNPDF3.1 set, we estimate a PDF uncertainty of 3.9 MeV. We find that the CT18 (61), MMHT2014 (62), and NNPDF3.1 NNLO PDF sets produce consistent results for the W boson mass, within ±2.1 MeV of the midpoint of the interval spanning the range of

Parton Distribution Functions (PDFs)

- Affect W boson kinematic line-shapes through acceptance cuts

- We use NNPDF3.1 as the default NNLO PDFs

- Use ensemble of 25 'uncertainty' PDFs => 3.9 MeV

  - Represent variations of eigenvectors in the PDF parameter space

  - compute δM_W contribution from each error PDF

- Central values from NNLO PDF sets CT18, MMHT2014 and NNPDF3.1 agree within 2.1 MeV of their midpoint

- As an additional check, central values from NLO PDF sets ABMP16, CJ15, MMHT2014 and NNPDF3.1 agree within 3 MeV of their midpoint

- Missing higher-order QCD effects estimated to be 0.4 MeV

  - varying the factorization and renormalization scales

  - comparing two event generators with different resummation and non-perturbative schemes.
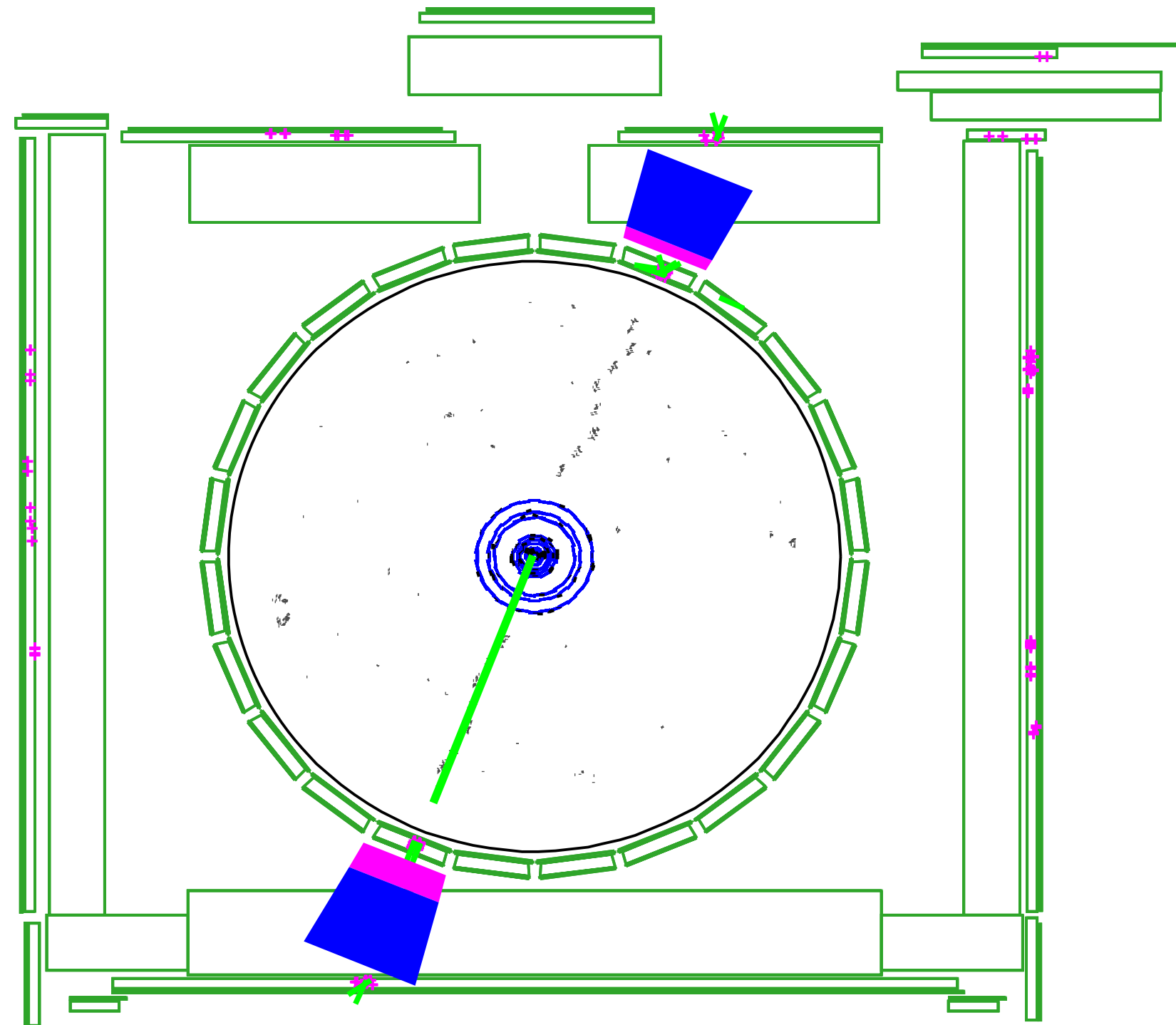
A. V. Kotwal, SLAC, 4/11/22

COT alignment

values. The model-dependent i
analysis implies that future impi
corrections in any relevant theor
ing can be used to update our measurement
quantifiably [see section IV of (*63*)].

The custom simulation includes a detailed
calculation of the lepton and photon interactions
in the detector (*39, 43, 64*), as well as models
describing their individual position measure-
ments within the COT. The COT position reso-
lution as a function of radius is determined
using muon tracks from Υ meson, W boson,
and Z boson decays. All wire positions in the
COT are measured with 1-um precision using
an in situ sample of cosmic ray muons (*65*), in
addition to the electron tracks from W boson
decays. The difference between electron and
positron track momenta relative to their
measured energy in the calorimeter (which
is independent of charge) strongly constrains
certain modes of internal misalignment in
the COT.

Momentum and energy calibration

The track momentum measurement in the
COT is calibrated by measuring the masses
of the J/ψ and $\Upsilon(1S)$ mesons reconstructed

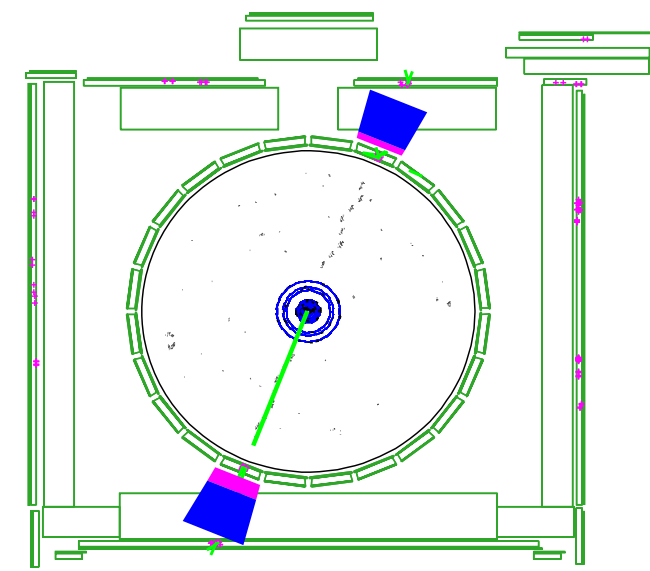Use a clean sample of ~480k cosmic rays
for cell-by-cell internal alignment

values. The model-dependent r
analysis implies that future impr
corrections in any relevant theor
ing can be used to update our measurement
quantifiably [see section IV of (*63*)].

The custom simulation includes a detailed
calculation of the lepton and photon interactions
in the detector (*39, 43, 64*), as well as models
describing their individual position measure-
ments within the COT. The COT position reso-
lution as a function of radius is determined
using muon tracks from Υ meson, *W* boson,
and *Z* boson decays. All wire positions in the
COT are measured with 1-μm precision using
an in situ sample of cosmic ray muons (*65*), in
addition to the electron tracks from *W* boson
decays. The difference between electron and
positron track momenta relative to their
measured energy in the calorimeter (which
is independent of charge) strongly constrains
certain modes of internal misalignment in
the COT.

Momentum and energy calibration

The track momentum measurement in the
COT is calibrated by measuring the masses
of the *J*/ψ and Υ(1S) mesons reconstructed

Residuals of COT cells after alignment

(AVK & CH, *NIM A* 762 (2014) pp 85-99)

before alignment

after alignment

Final relative alignment of cells ~1 μm (initial alignment ~50 μm)

COT alignment

values. The model-dependent residual analysis implies that future improved corrections in any relevant theoretical modeling can be used to update our measurement quantifiably [see section IV of (63)].

The custom simulation includes a detailed calculation of the lepton and photon interactions in the detector (39, 43, 64), as well as models describing their individual position measurements within the COT. The COT position resolution as a function of radius is determined using muon tracks from Υ meson, W boson, and Z boson decays. All wire positions in the COT are measured with 1-μm precision using an in situ sample of cosmic ray muons (65), in addition to the electron tracks from W boson decays. The difference between electron and positron track momenta relative to their measured energy in the calorimeter (which is independent of charge) strongly constrains certain modes of internal misalignment in the COT.
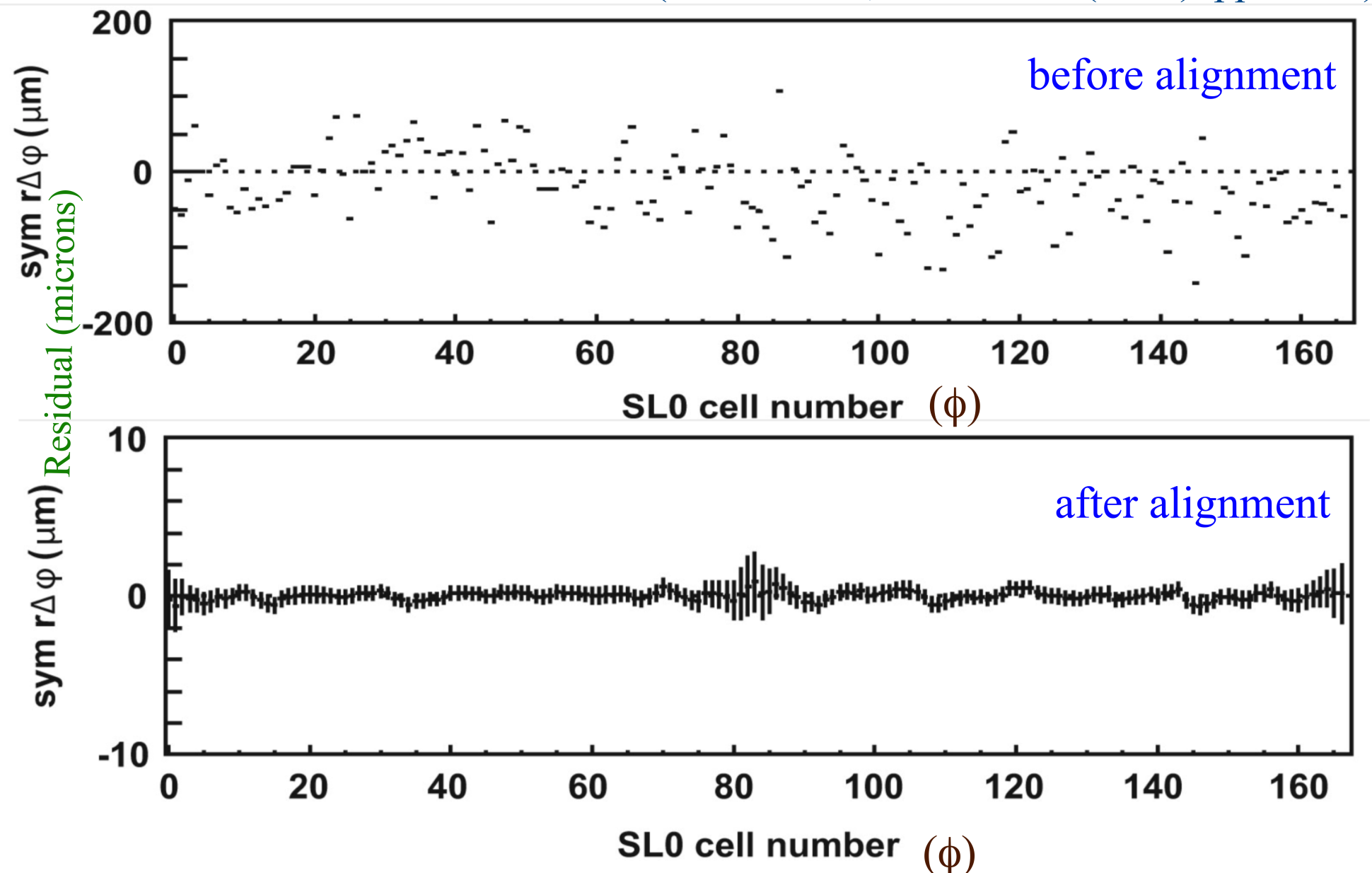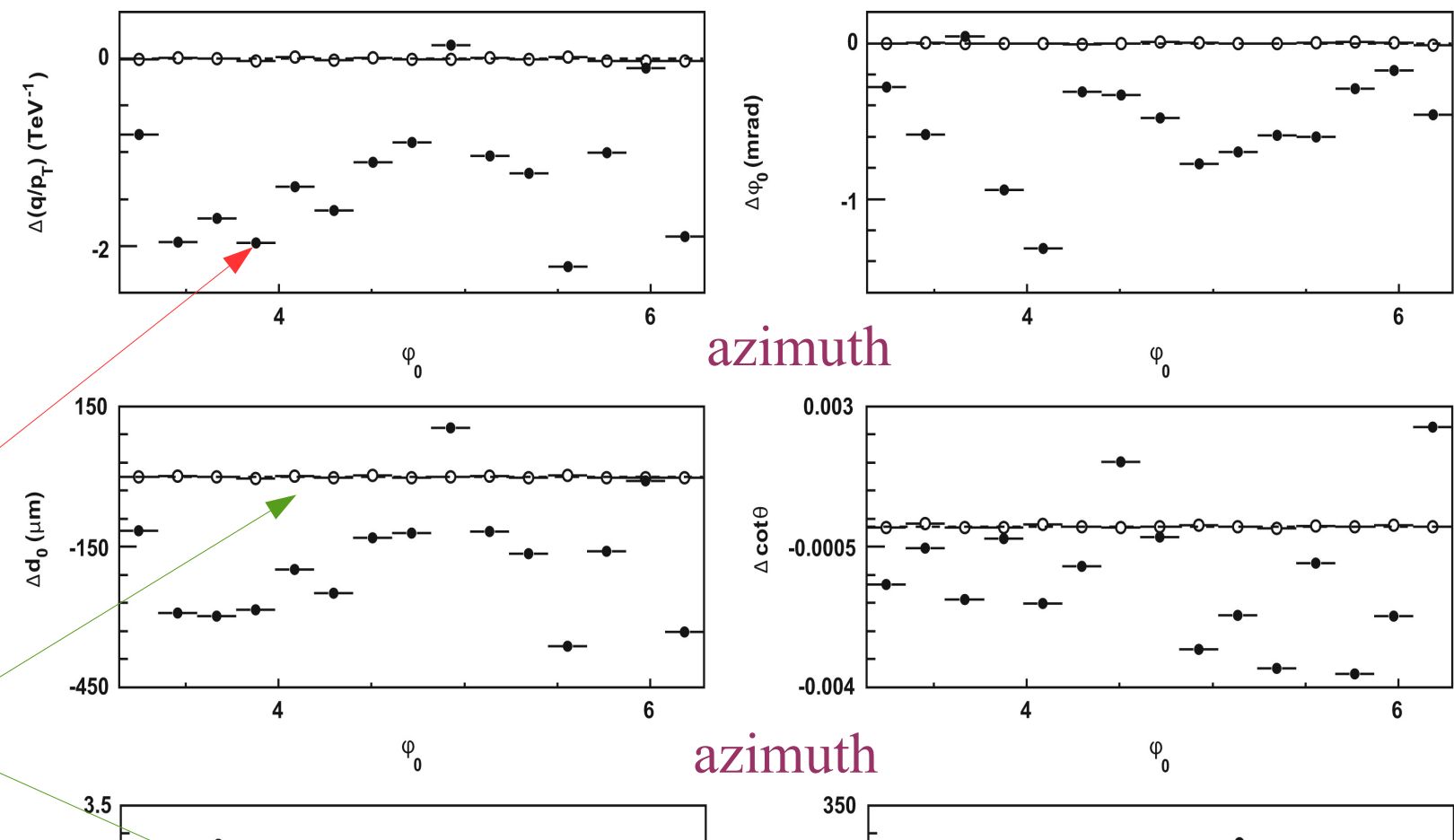
Momentum and energy calibration

The track momentum measurement in the COT is calibrated by measuring the masses of the J/ψ and $\Upsilon(1S)$ mesons reconstructed

Residuals of COT cells after alignment

(AVK & CH, *NIM A* 762 (2014) pp 85-99)

before alignment

after alignment

Final relative alignment of cells ~1 μm (initial alignment ~50 μm)

A. V. Kotwal, SLAC, 4/11/22   23

track parameter bias versus azimuth

azimuth

solid = before alignment

open = after alignment

azimuth

consistency check of COT alignment

certain modes of internal misalignment in the COT.

Momentum and energy calibration

The track momentum measurement in the COT is calibrated by measuring the masses of the J/ψ and $\Upsilon(1S)$ mesons reconstructed in their dimuon decays and comparing them with the known values (10). These meson mass measurements are performed with maximum-likelihood fits to the dimuon mass distributions from data, using templates obtained from the custom simulation. Measurements of these masses as functions of muon momenta are used to correct for small inaccuracies in the magnetic field map, the COT position measurements, and the modeling of the energy loss by particles traversing the detector. A mismodeling of the energy loss would lead to a bias linear in the mean inverse p_T of the two muons. No such bias is observed after applying the magnetic field nonuniformity, COT, and energy-loss corrections (Fig. 2A). The curvature q/p_T measured by the COT, where q is the particle charge, is an analytic function of the true curvature. The curvature response function analytically yields a linear dependence of the measured invariant mass on p_T^{-1} and

$\vec{p}, E$ calibration

$\Delta M_W = 2$ MeV

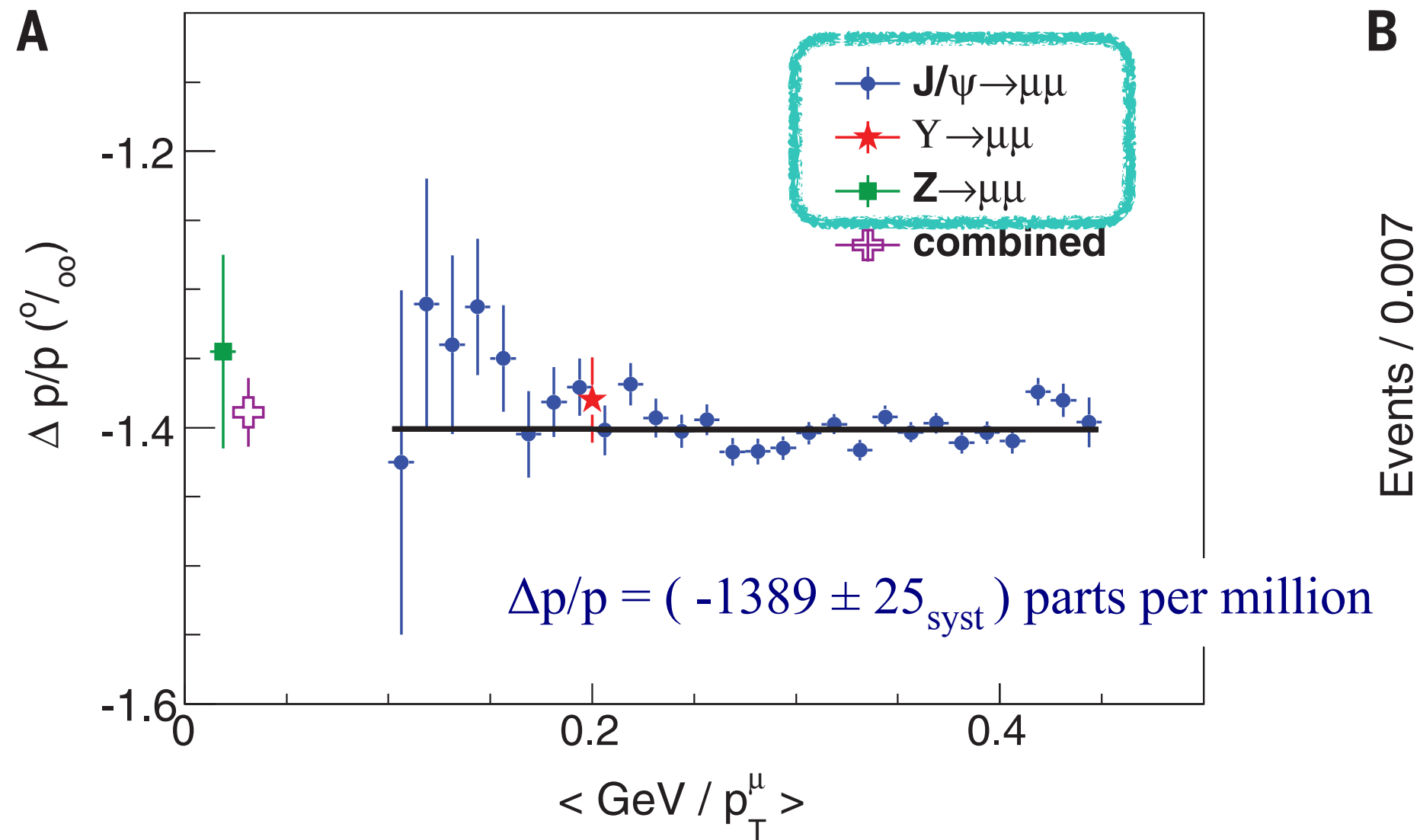$\Delta p/p = (-1389 \pm 25_{syst})$ parts per million

Fig. 2. Calibration of track momentum and electron's calorimeter energy.
(**A**) Fractional deviation of momentum $\Delta p/p$ (per mille) extracted from fits to the $J/\psi \to \mu\mu$ resonance peak as a function of the mean muon unsigned curvature $\langle 1/p_T^\mu \rangle$ (blue circles). A linear fit to the points, shown in black, has a slope consistent with zero (17 ± 34 keV). The corresponding values of $\Delta p/p$ extracted from fits to the $\Upsilon \to \mu\mu$ and $Z \to \mu\mu$ resonance peaks are also shown. The combination of all of these $\Delta p/p$ measurements yields the momentum correction labeled "combined," which is applied to the lepton tracks in W boson data. Error bars indicate the

uncorrel
(combin
the best
misreco
the elec
the calib
In this a
agreeme

$\vec{p}$, E **calibration**

Momentum and energy calibration

The track momentum measurement in the COT is calibrated by measuring the masses of the J/ψ and $\Upsilon(1S)$ mesons reconstructed in their dimuon decays and comparing them with the known values (*10*). These meson mass measurements are performed with maximum-likelihood fits to the dimuon mass distributions from data, using templates obtained from the custom simulation. Measurements of these masses as functions of muon momenta are used to correct for small inaccuracies in the magnetic field map, the COT position measurements, and the modeling of the energy loss by particles traversing the detector. A mismodeling of the energy loss would lead to a bias linear in the mean inverse p_T of the two muons. No such bias is observed after applying the magnetic field nonuniformity, COT, and energy-loss corrections (Fig. 2A). The curvature q/p_T measured by the COT, where q is the particle charge, is an analytic function of the true curvature. The curvature response function analytically yields a linear dependence of the measured invariant mass on p_T^{-1}, and higher-order terms in p_T^{-1} are negligible. The correction for the fractional deviation of the measured momentum from its correct value, $\Delta p/p = p_{\text{measured}}/p_{\text{true}} - 1$, is inferred from the comparison of the measured meson masses to their more-precise world-average masses. The $\Delta p/p$ corrections extracted from the individual J/ψ and $\Upsilon(1S)$ invariant mass fits are consistent with each other, and the results are combined to obtain $\Delta p/p = (-1393 \pm 26)$ parts per million (ppm).

The combined momentum calibration is used to measure the Z boson mass in the dimuon channel (Fig. 3A), which is blinded with a random offset in the range of −50 to 50 MeV until all analysis procedures are established. The unblinded measurement is $M_Z = 91{,}192.0 \pm 6.4_{\text{stat}} \pm 4.0_{\text{syst}}$ MeV (stat, statistical uncertainty; syst, systematic uncertainty), which is consistent with the world average of $91{,}187.6 \pm 2.1$ MeV (*10, 44*) and therefore provides a precise consistency check. Systematic uncertainties on M_Z result from uncertainties on the longitudinal coordinate measurements in the COT (1.0 MeV), the momentum calibration (2.3 MeV), and the QED radiative corrections (3.1 MeV). The latter two sources are correlated with the M_W measurement. The $Z \to \mu\mu$ mass measurement is then included in the final momentum calibration. The systematic uncertainties stemming from the magnetic field nonuniformity dominate the total uncertainty of 25 ppm in the combined momentum calibration.

After track momentum (p) calibration, the electron's calorimeter energy (E) is calibrated using the peak of the E/p distribution in $W \to e\nu$ (Fig. 2B) and $Z \to ee$ [fig. S13 in (*63*)] data. Fits to this peak in bins of electron E_T determine the electron energy calibration and its dependence on E_T. The radiative region of the E/p distribution ($E/p > 1.12$) is fitted to
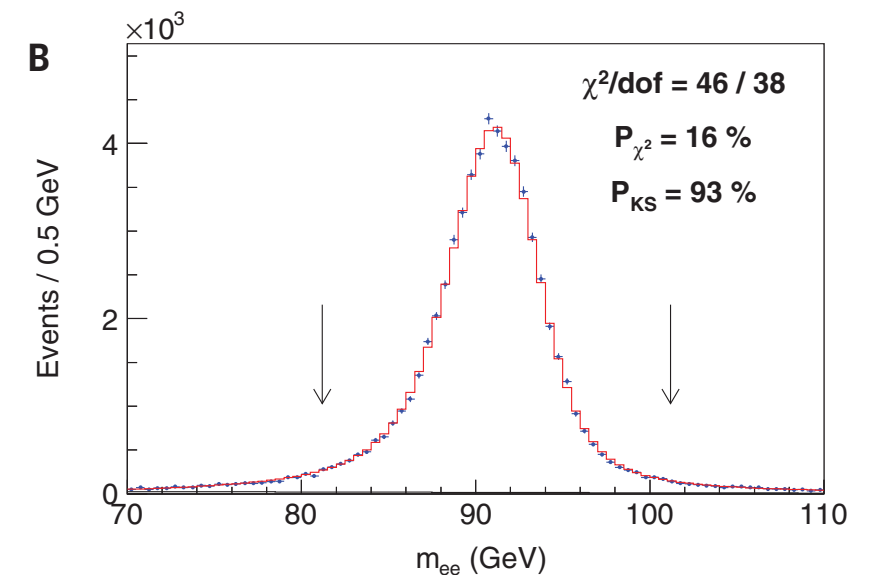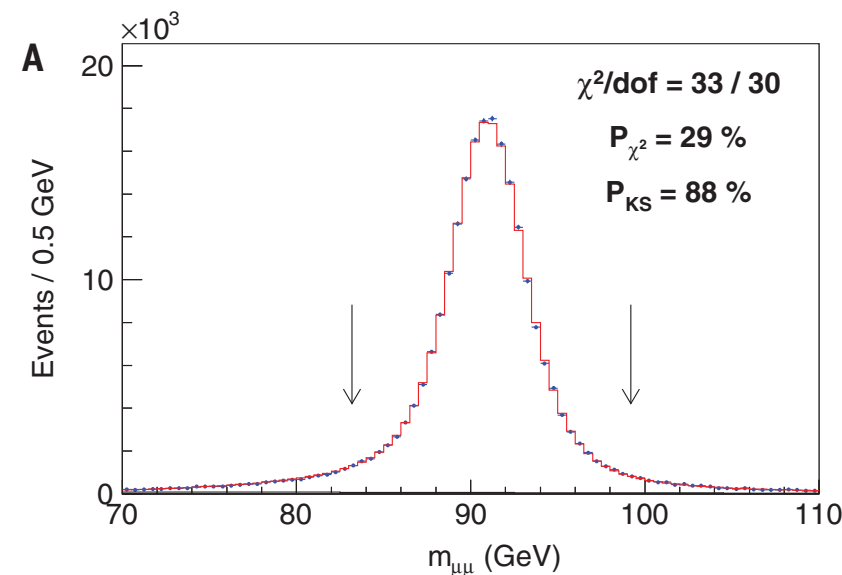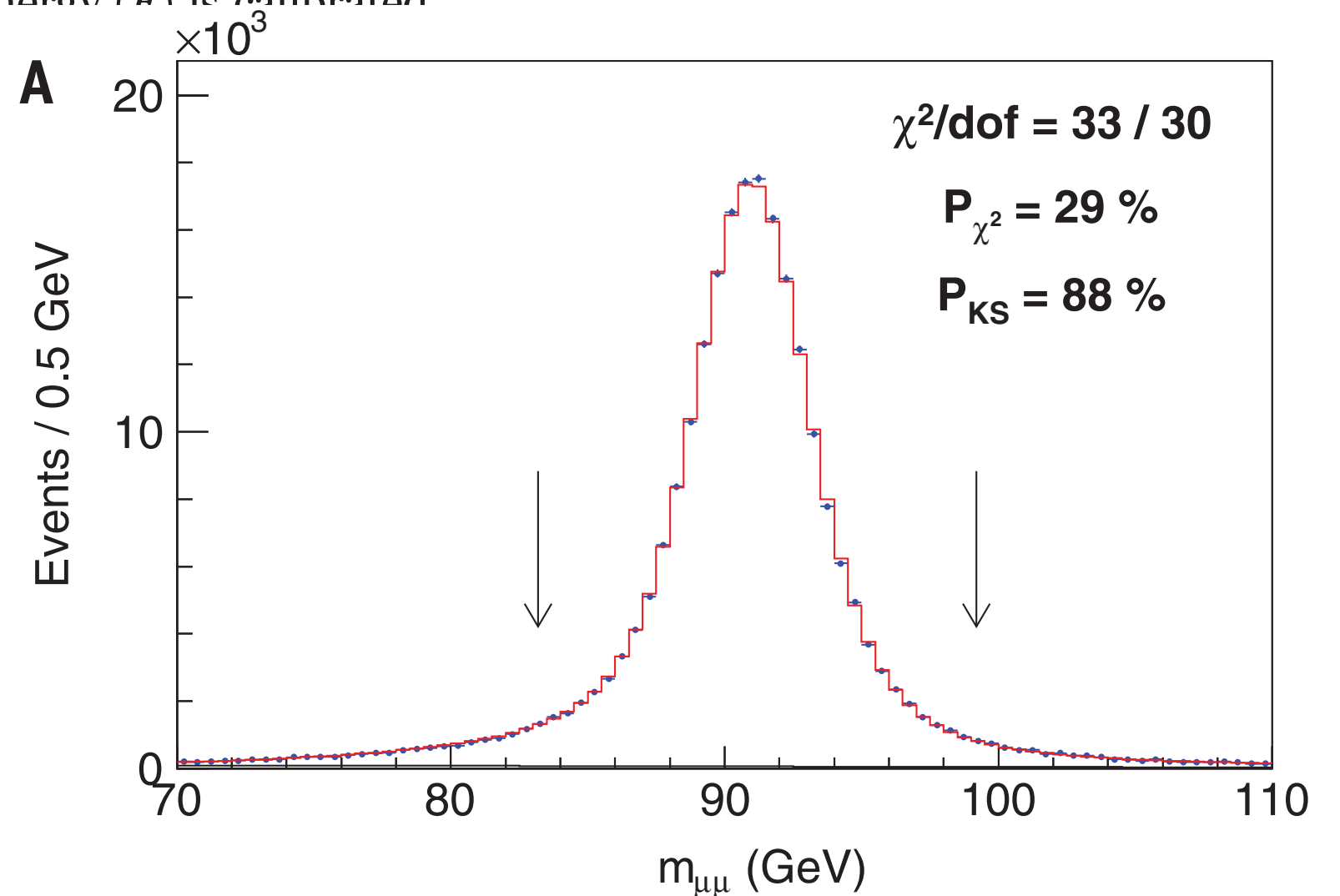
$\vec{p}, E$ **calibration**

are combined to obtain $\Delta p/p = (-1393 \pm 26)$ parts per million (ppm).

The combined momentum calibration is used to measure the Z boson mass in the dimuon channel (Fig. 3A), which is blinded with a random offset in the range of −50 to 50 MeV until all analysis procedures are established. The unblinded measurement is $M_Z = 91{,}192.0 \pm 6.4_{\text{stat}} \pm 4.0_{\text{syst}}$ MeV (stat, statistical uncertainty; syst, systematic uncertainty), which is consistent with the world average of $91{,}187.6 \pm 2.1$ MeV (*10, 44*) and therefore provides a precise consistency check. Systematic uncertainties on M_Z result from uncertainties on the longitudinal coordinate measurements in the COT (1.0 MeV), the momentum calibration (2.3 MeV), and the

QED radiative corrections (3.1 MeV). The latter two sources are correlated with the M_W measurement. The $Z \rightarrow \mu\mu$ mass measurement is then included in the final momentum calibration. The systematic uncertainties stemming from the magnetic field nonuniformity dominate the total uncertainty of 25 ppm in the combined momentum calibration.

After track momentum (p) calibration, the electron's calorimeter energy (E) is calibrated using the peak of the $W \rightarrow e\nu$ (Fig. 2B) and Z data. Fits to this peak determine the electron its dependence on E_{T}. the E/p distribution (

$\vec{p}, E$ **calibration**
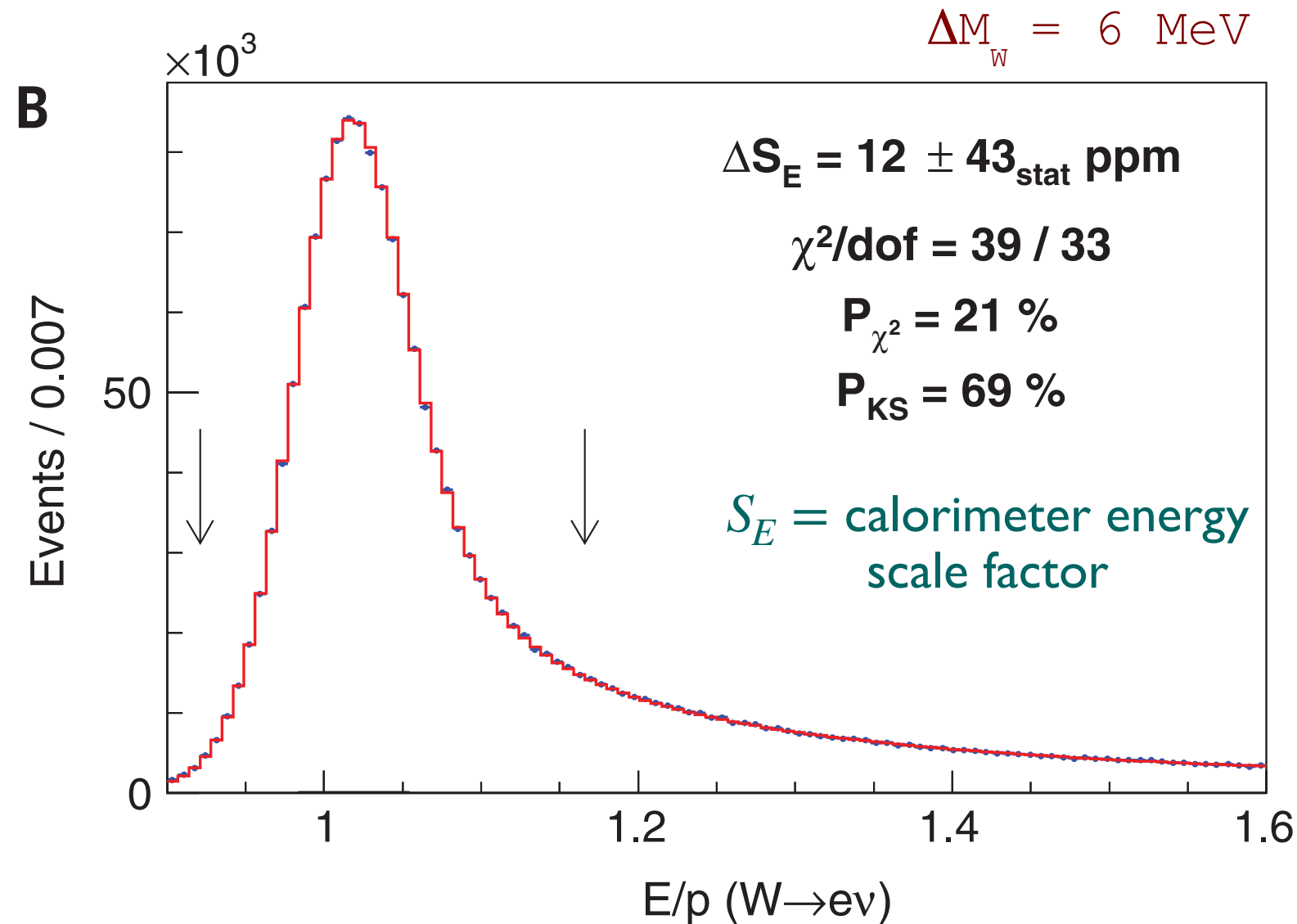

channel (Fig. 3A), which is blinded with a random offset in the range of –50 to 50 MeV until all analysis procedures are established. The unblinded measurement is $M_Z = 91{,}192.0 \pm 6.4_{stat} \pm 4.0_{syst}$ MeV (stat, statistical uncertainty; syst, systematic uncertainty), which is consistent with the world average of $91{,}187.6 \pm 2.1$ MeV (*10, 44*) and therefore provides a precise consistency check. Systematic uncertainties on M_Z result from uncertainties on the longitudinal coordinate measurements in the COT (1.0 MeV), the momentum calibration (2.3 MeV), and the

QED radiative corrections (3.1 MeV). The latter two sources are correlated with the M_W measurement. The $Z \rightarrow \mu\mu$ mass measurement is then included in the final momentum calibration. The systematic uncertainties stemming from the magnetic field nonuniformity dominate the total uncertainty of 25 ppm in the combined momentum calibration.

   After track momentum (p) calibration, the electron's calorimeter energy (E) is calibrated using the peak of the E/p distribution in $W \rightarrow e\nu$ (Fig. 2B) and $Z \rightarrow ee$ [fig. S13 in (*63*)] data. Fits to this peak in bins of electron E_T determine the electron energy calibration and its dependence on E_T. The radiative region of the E/p distribution ($E/p > 1.12$) is fitted to

$\Delta M_W = 6$ MeV

B

$\times 10^3$

$\Delta S_E = 12 \pm 43_{stat}$ **ppm**

$\chi^2/\mathrm{dof} = 39 / 33$

$P_{\chi^2} = 21\ \%$

$P_{KS} = 69\ \%$

$S_E =$ calorimeter energy scale factor

Events / 0.007

E/p (W→eν)

uncorrelated uncertainties (total uncertainty) for the individual boson measurements (combined correction). (**B**) Distribution of E/p for the $W \rightarrow e\nu$ data (points) and the best-fit simulation (histogram) including the small background from hadrons misreconstructed as electrons. The arrows indicate the fitting range used for the electron energy calibration. The relative energy correction ΔS_E, averaged over the calibrated W and Z boson data [see fig. S13 in (*63*)], is compatible with zero. In this and other figures, P_{KS} refers to the Kolmogorov-Smirnov probability of agreement between the shapes of the data and simulated distributions.

channel (Fig. 3A), which is blinded with a random offset in the range of −50 to 50 MeV until all analysis procedures are established. The unblinded measurement is $M_Z = 91{,}192.0 \pm 6.4_{\text{stat}} \pm 4.0_{\text{syst}}$ MeV (stat, statistical uncertainty; syst, systematic uncertainty), which is consistent with the world average of $91{,}187.6 \pm 2.1$ MeV (10, 44) and therefore provides a precise consistency check. Systematic uncertainties on M_Z result from uncertainties on the longitudinal coordinate measurements in the COT (1.0 MeV), the momentum calibration (2.3 MeV), and the QED radiative corrections (3.1 MeV). The latter two sources are correlated with the M_W measurement. The $Z \to \mu\mu$ mass measurement is then included in the final momentum calibration. The systematic uncertainties stemming from the magnetic field nonuniformity dominate the total uncertainty of 25 ppm in the combined momentum calibration.

After track momentum (p) calibration, the electron's calorimeter energy (E) is calibrated using the peak of the E/p distribution in $W \to e\nu$ (Fig. 2B) and $Z \to ee$ [fig. S13 in (63)] data. Fits to this peak in bins of electron E_T determine the electron energy calibration and its dependence on E_T. The radiative region of the E/p distribution ($E/p > 1.12$) is fitted to

$\vec{p}, E$ **calibration**

FIG. S13: (Left) Measured calorimeter energy scale in bins of electron tower in $W \to e\nu$ data after corrections are applied, with the line $S_E = 1$ overlaid. The towers are numbered in order of increasing $|\eta|$ and each tower subtends $\Delta\eta \approx 0.11$. (Right) Distribution of E/p for $Z \to ee$ data (circles) after the full energy-scale calibration; the best-fit template (histogram) is overlaid. The fit region is enclosed by arrows.

Youngjoo

channel (Fig. 3A), which is blinded with a random offset in the range of –50 to 50 MeV until all analysis procedures are established. The unblinded measurement is $M_Z = 91{,}192.0 \pm 6.4_{\text{stat}} \pm 4.0_{\text{syst}}$ MeV (stat, statistical uncertainty; syst, systematic uncertainty), which is consistent with the world average of $91{,}187.6 \pm 2.1$ MeV (*10, 44*) and therefore provides a precise consistency check. Systematic uncertainties on M_Z result from uncertainties on the longitudinal coordinate measurements in the COT (1.0 MeV), the momentum calibration (2.3 MeV), and the

QED radiative corrections (3.1 MeV). The latter two sources are correlated with the M_W measurement. The $Z \to \mu\mu$ mass measurement is then included in the final momentum calibration. The systematic uncertainties stemming from the magnetic field nonuniformity dominate the total uncertainty of 25 ppm in the combined momentum calibration.

After track momentum (p) calibration, the electron's calorimeter energy (E) is calibrated using the peak of the E/p distribution in $W \to e\nu$ (Fig. 2B) and $Z \to ee$ [fig. S13 in (*63*)] data. Fits to this peak in bins of electron E_T determine the electron energy calibration and its dependence on E_T. The radiative region of the E/p distribution ($E/p > 1.12$) is fitted to

$\vec{p}, E$ **calibration**
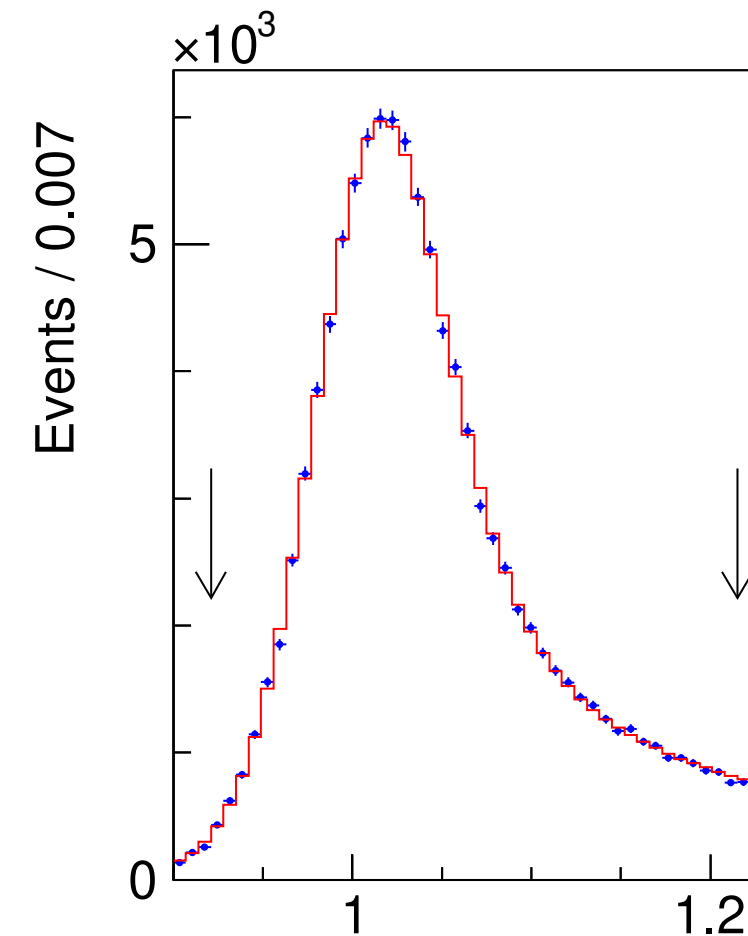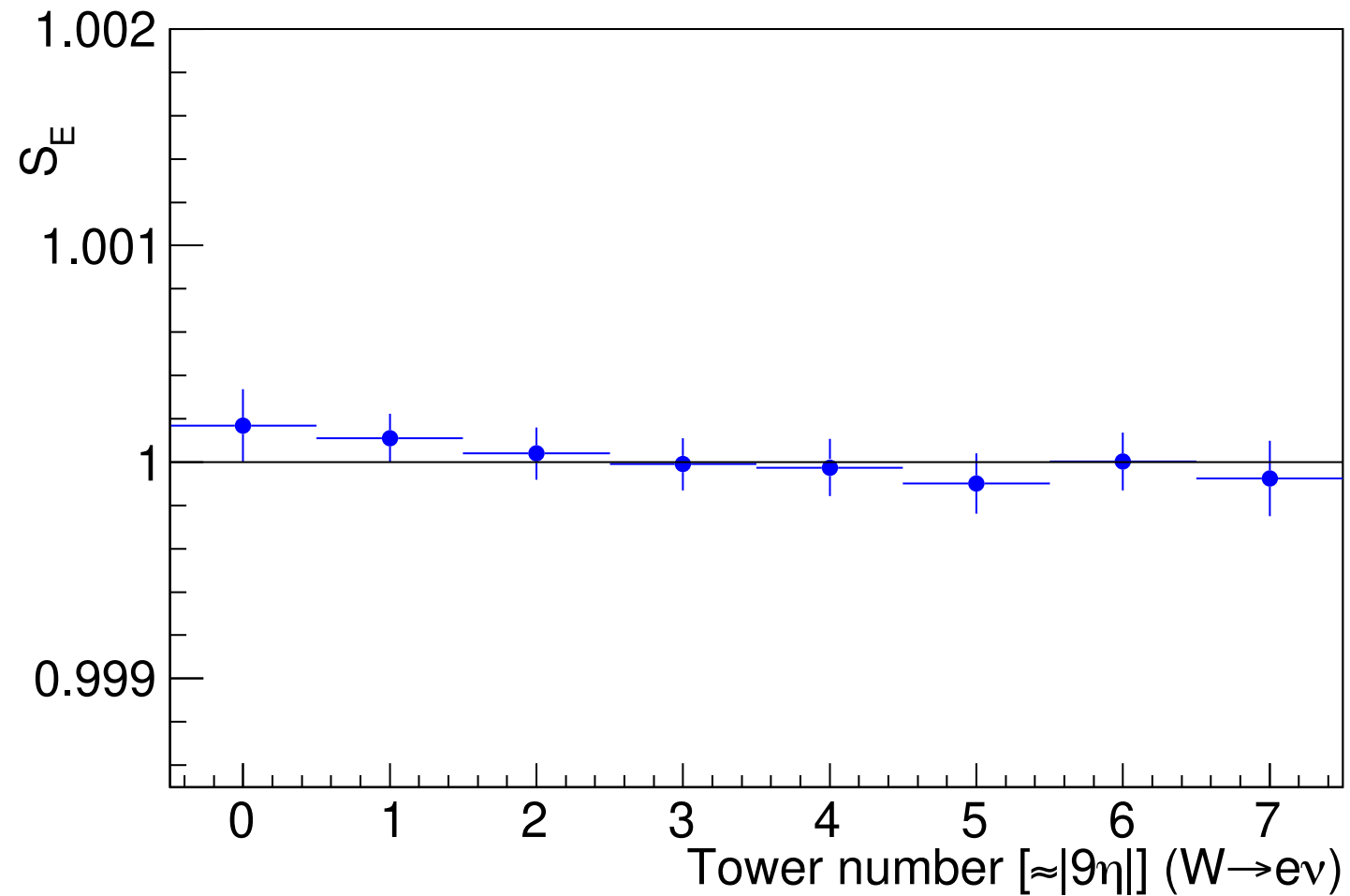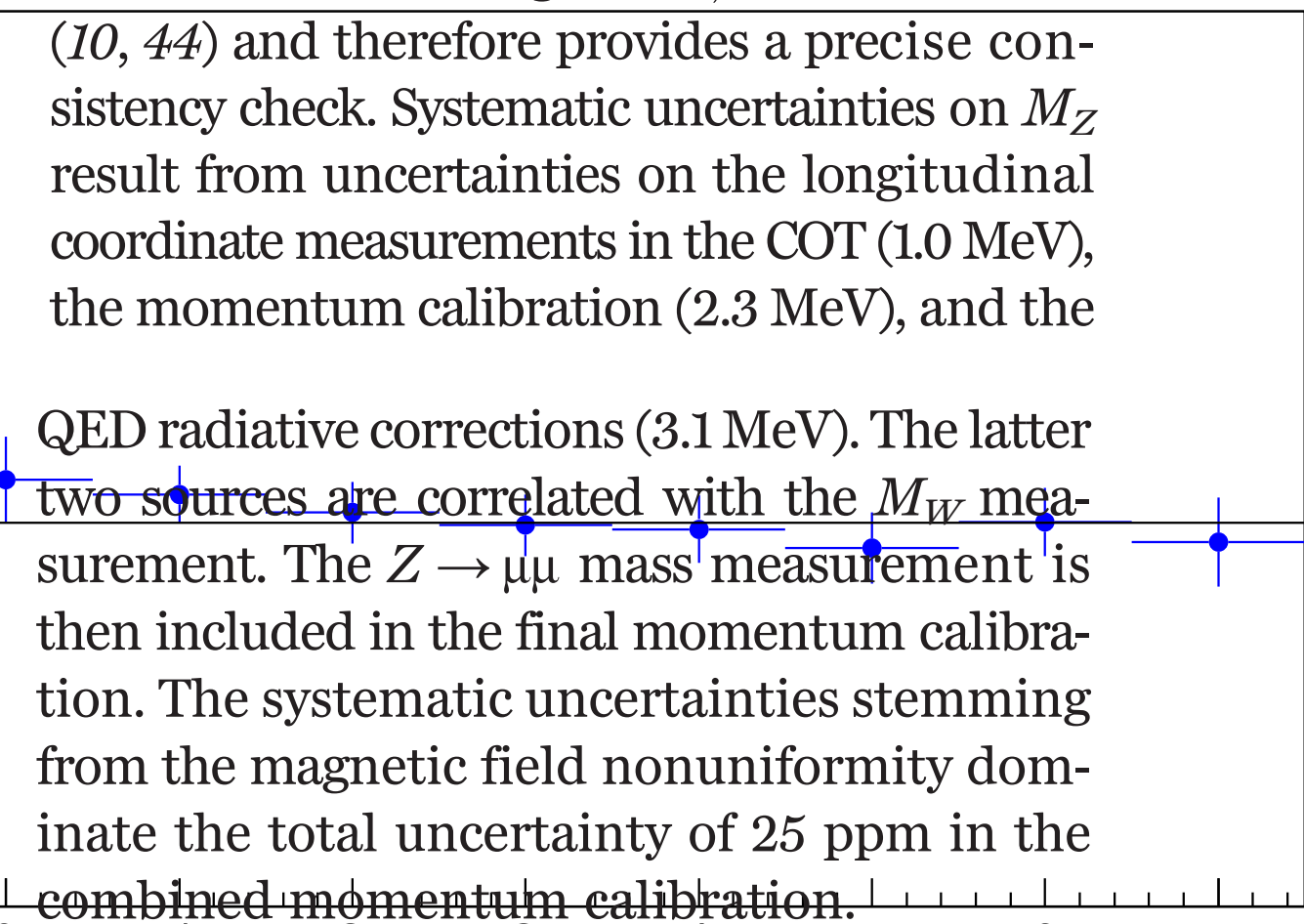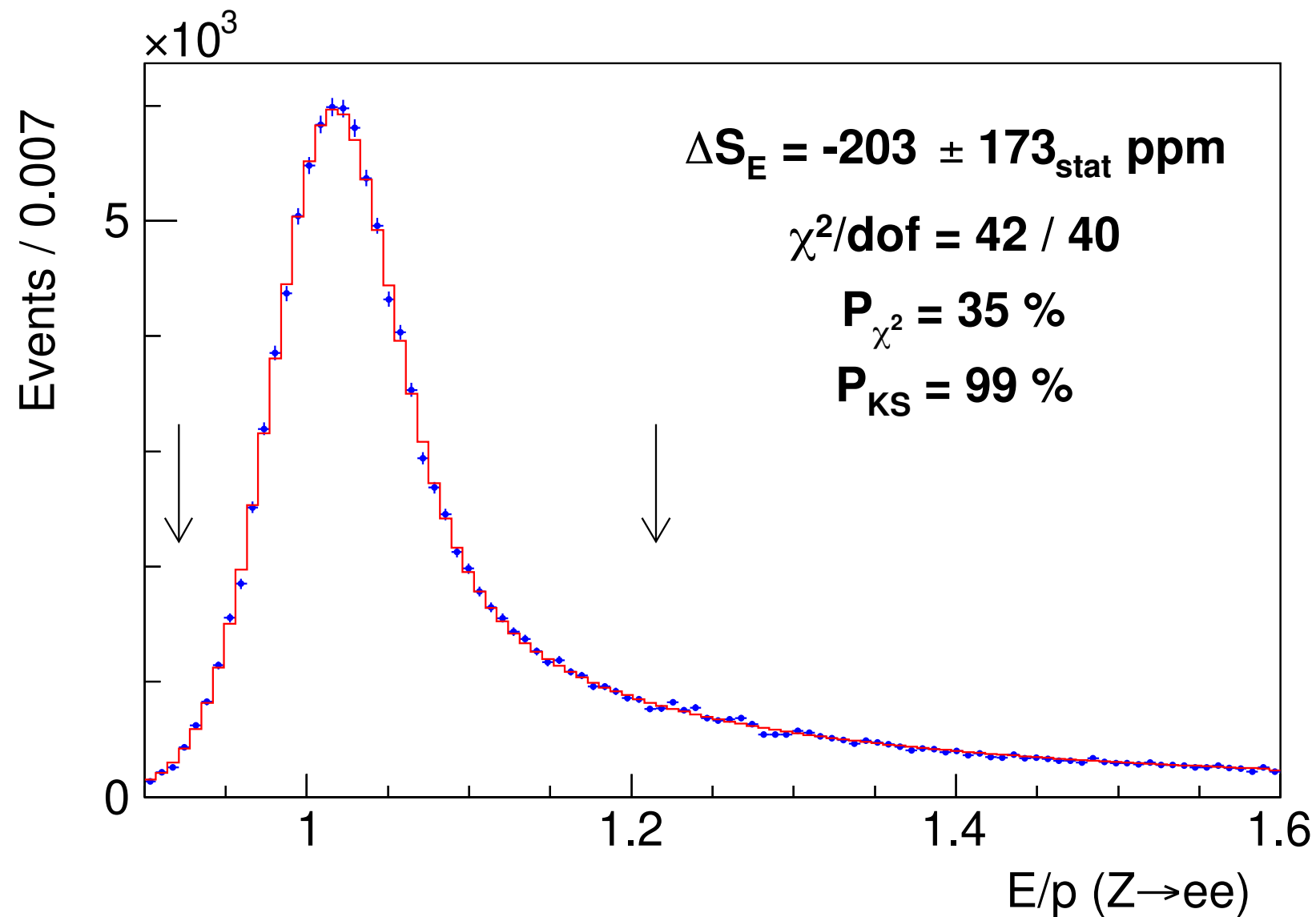

FIG. S13: (Left) Measured calorimeter energy scale in bins of electron tower in $W \to e\nu$ data after corrections are applied, with the line $S_E = 1$ overlaid. The towers are numbered in order of increasing $|\eta|$ and each tower subtends $\Delta\eta \approx 0.11$. (Right) Distribution of E/p for $Z \to ee$ data (circles) after the full energy-scale calibration; the best-fit template (histogram) is overlaid. The fit region is enclosed by arrows.

$\Delta S_E = -203 \pm 173_{\text{stat}}$ ppm

$\chi^2/\text{dof} = 42 / 40$

$P_{\chi^2} = 35 \%$

$P_{\text{KS}} = 99 \%$

$\Delta S_{\text{mat}} = 0.05 \pm 0.16_{\text{stat}} \%$

$\chi^2/\text{dof} = 3.1 / 2$

$P_{\chi^2} = 20 \%$

$\Delta S_{\text{mat}} = -0.6 \pm 0.6_{\text{stat}} \%$

$\chi^2/\text{dof} = 4.2 / 2$

$P_{\chi^2} = 12 \%$

22

$\overrightarrow{p}, E$ **calibration**

then included in the final momentum calibration. The systematic uncertainties stemming from the magnetic field nonuniformity dominate the total uncertainty of 25 ppm in the combined momentum calibration.

After track momentum (p) calibration, the electron's calorimeter energy (E) is calibrated using the peak of the E/p distribution in $W \to e\nu$ (Fig. 2B) and $Z \to ee$ [fig. S13 in (63)] data. Fits to this peak in bins of electron E_T determine the electron energy calibration and its dependence on E_T. The radiative region of the E/p distribution ($E/p > 1.12$) is fitted to measure a small correction ($\approx 5\%$) to the amount of radiative material traversed in the tracking volume. The EM calorimeter resolution is measured using the widths of the E/p peak in the $W \to e\nu$ sample and of the mass peak of the $Z \to ee$ sample.

We use the calibrated electron energies to measure the Z boson mass in the dielectron channel (Fig. 3B), which is also blinded with the same offset as used for the dimuon channel. The unblinded result, $M_Z = 91{,}194.3 \pm 13.8_{stat} \pm 7.6_{syst}$ MeV, is consistent with the world average, providing a stringent consistency check of the electron energy calibration. Systematic uncertainties on M_Z are caused by uncertainties on the calorimeter energy
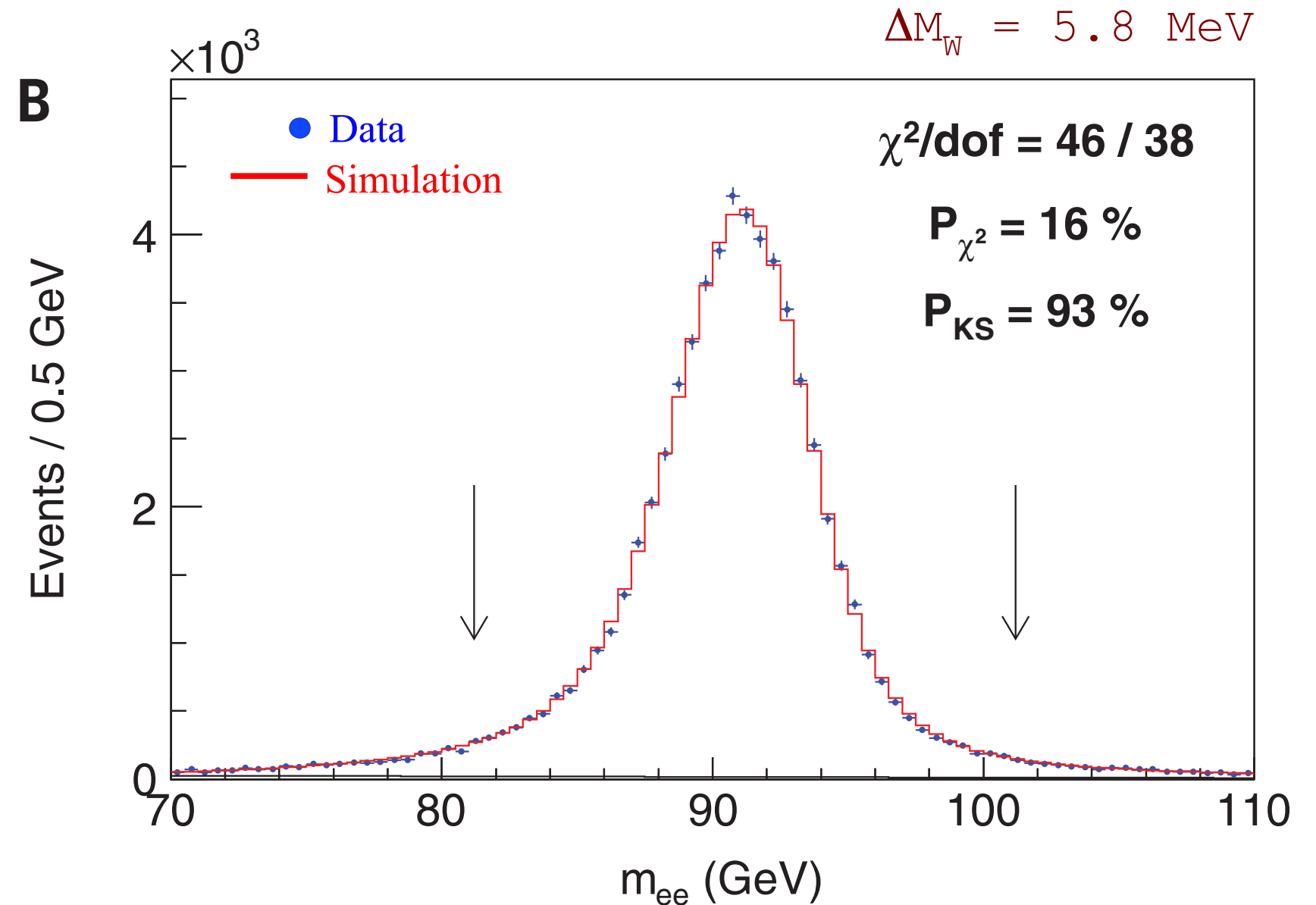

$\Delta M_W = 5.8$ MeV

$\chi^2/dof = 46 / 38$

$P_{\chi^2} = 16\%$

$P_{KS} = 93\%$

Fig. 3. Decay of the Z boson. (**A** and **B**) Distribution of (A) dimuon and (B) dielectron mass for candidate $Z \to \mu\mu$ and $Z \to ee$ decays, respectively. The data (points) are overlaid with the best-fit simulation template including the photon-mediated contribution (histogram). The arrows indicate the fitting range.

surement. The $Z \to \mu\mu$ mass measurement is then included in the final momentum calibration. The systematic uncertainties stemming from the magnetic field nonuniformity dominate the total uncertainty of 25 ppm in the combined momentum calibration.
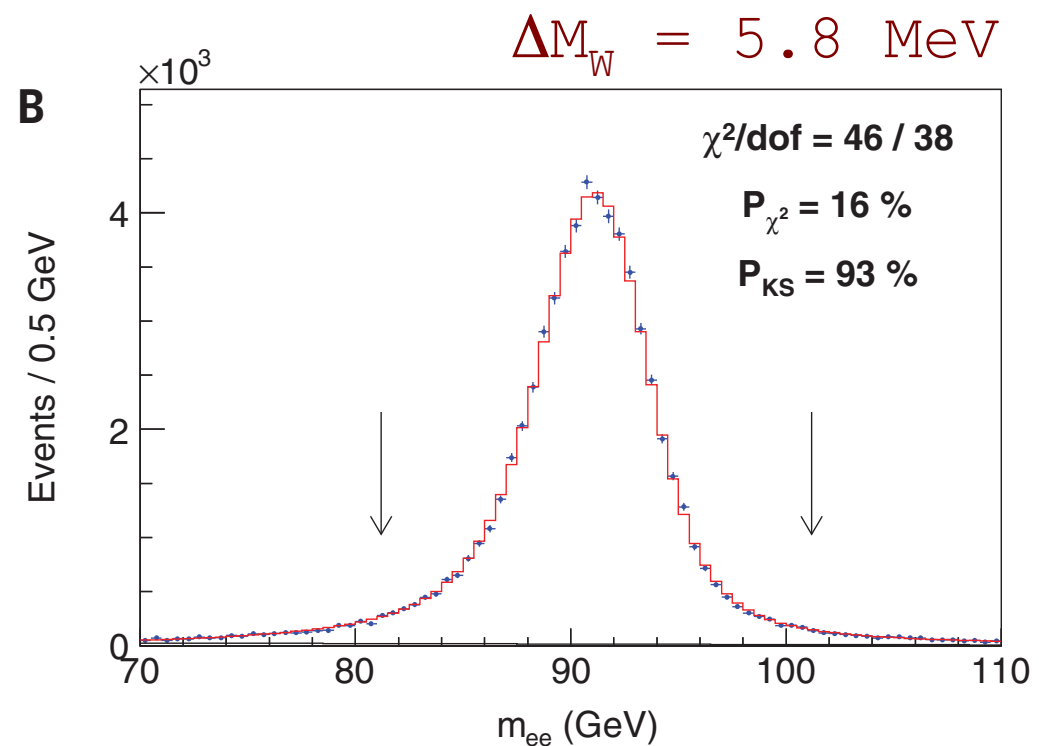
After track momentum (p) calibration, the electron's calorimeter energy (E) is calibrated using the peak of the E/p distribution in $W \to e\nu$ (Fig. 2B) and $Z \to ee$ [fig. S13 in (63)] data. Fits to this peak in bins of electron E_T determine the electron energy calibration and its dependence on E_T. The radiative region of the E/p distribution ($E/p > 1.12$) is fitted to measure a small correction ($\approx 5\%$) to the amount of radiative material traversed in the tracking volume. The EM calorimeter resolution is measured using the widths of the E/p peak in the $W \to e\nu$ sample and of the mass peak of the $Z \to ee$ sample.

We use the calibrated electron energies to measure the Z boson mass in the dielectron channel (Fig. 3B), which is also blinded with the same offset as used for the dimuon channel. The unblinded result, $M_Z = 91{,}194.3 \pm 13.8_{stat} \pm 7.6_{syst}$ MeV, is consistent with the world average, providing a stringent consistency check of the electron energy calibration. Systematic uncertainties on M_Z are caused by uncertainties on the calorimeter energy

$\vec{p}, E$ calibration

(6.5 MeV) and track momentum (2.3 MeV), on the z coordinate measured in the COT (0.8 MeV), and on QED radiative corrections (3.1 MeV). Measurements of the Z boson mass using the dielectron track momenta, and comparisons of mass measurements using radiative and nonradiative electrons, provide consistent results. The final calibration of the electron energy is obtained by combining the E/p-based calibration with the $Z (\to ee)$ mass-based calibration, taking into account the correlated uncertainty on the radiative corrections.
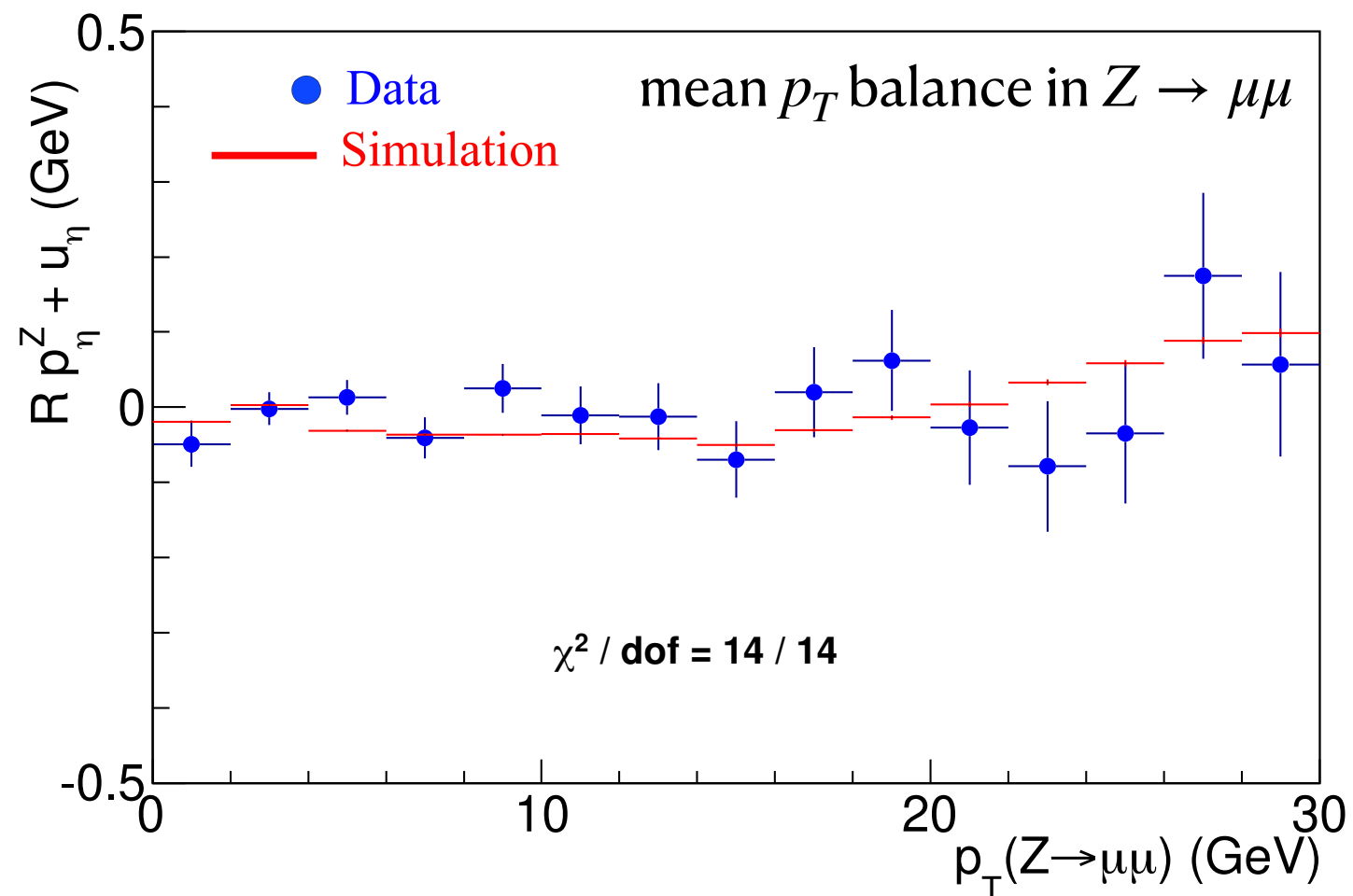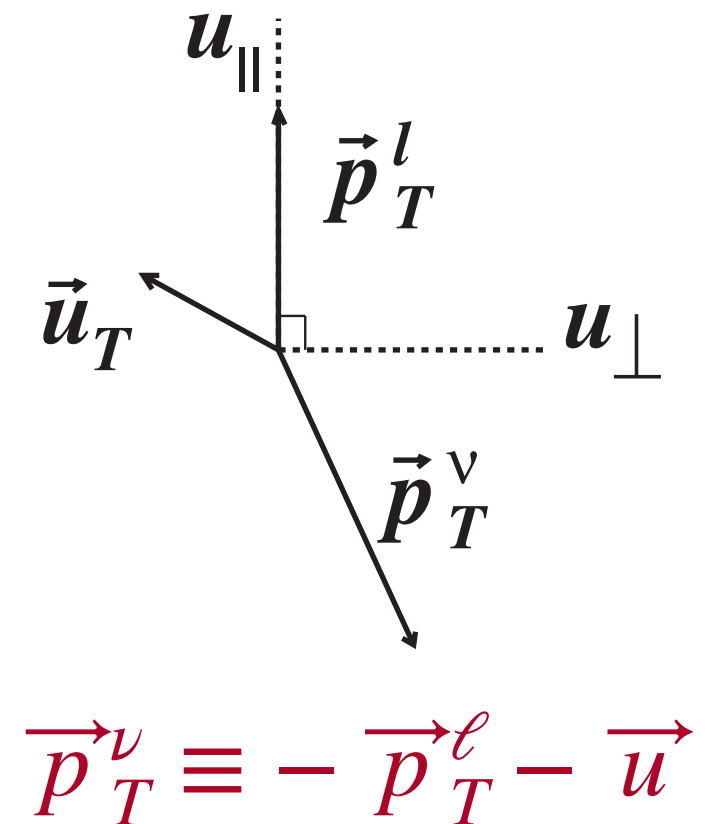
The spectator partons in the proton and antiproton, as well as the additional (≈ 3) $p\bar{p}$ interactions in the same collider bunch crossing, contribute visible energy that degrades the resolution of $\vec{u}$. These contributions are measured from events triggered on inelastic $p\bar{p}$ interactions and random bunch crossings, reproducing the collision environment of the W and Z boson data. Because there are no high-p_T neutrinos in the Z boson data, the $\vec{p}_T^{\,\ell\ell}$ imbalance between the $\vec{p}_T^{\,\ell\ell}$ and $\vec{u}$ in $Z \to \ell\ell$ events is used to measure the calorimeter response to, and resolution of, the initial-state QCD radiation accompanying boson production. The simulation of the recoil vector $\vec{u}$ also requires knowledge of the distribution of the energy flow into the calorimeter towers impacted by the leptons, because these towers are excluded from the computation of $\vec{u}$. This energy flow is measured from the W boson data using the event-averaged response of towers separated in azimuth from the lepton direction.

$$\Delta M_W = 5.8 \text{ MeV}$$

B

$\chi^2/\text{dof} = 46 / 38$

$P_{\chi^2} = 16\ \%$

$P_{KS} = 93\ \%$

Events / 0.5 GeV — m_{ee} (GeV)

$$\overrightarrow{p}, \overrightarrow{n}$$

The spectator partons in the proton and antiproton, as well as the additional (≈ 3) $p\bar{p}$ interactions in the same collider bunch crossing, contribute visible energy that degrades the resolution of $\vec{u}$. These contributions are measured from events triggered on inelastic $p\bar{p}$ interactions and random bunch crossings, reproducing the collision environment of the W and Z boson data. Because there are no high-p_{T} neutrinos in the Z boson data, the $\vec{p}_{\mathrm{T}}$ imbalance between the $\vec{p}_{\mathrm{T}}^{\,\ell\ell}$ and $\vec{u}$ in $Z \to \ell\ell$ events is used to measure the calorimeter response to, and resolution of, the initial-state QCD radiation accompanying boson production. The simulation of the recoil vector $\vec{u}$ also requires knowledge of the distribution of the energy flow into the calorimeter towers impacted by the leptons, because these towers are excluded from the computation of $\vec{u}$. This energy flow is measured from the W boson data using the event-averaged response of towers separated in azimuth from the lepton direction.

able collision products accompanying the W or Z boson is defined as the hadronic recoil $\vec{u} = \Sigma_i E_i \sin(\theta_i)\hat{n}_i$, where the sum is performed over calorimeter towers (52) with energy E_i, polar angle θ_i, and transverse directions specified by unit vectors $\hat{n}_i$. Calorimeter towers

$$\overrightarrow{p}_T^{\,\nu}$$

$$\overrightarrow{p}_T^{\,\nu} \equiv -\overrightarrow{p}_T^{\,\ell} - \overrightarrow{u}$$

χ^2 / dof = 14 / 14

mean p_T balance in $Z \to \mu\mu$

- Data
- Simulation

χ^2 / dof = 14 / 14

$\Delta M_W = 2$ MeV

ings, reproducing the collision environment of the W and Z boson data. Because there are no $\vec{p}_T$ eve response to, and resolution of, the initial-state QCD radiation accompanying boson production. The simulation of the recoil vector $\vec{u}$ also requires knowledge of the distribution of the energy flow into the calorimeter towers impacted by the leptons, because these towers are excluded from the computation of $\vec{u}$. This energy flow is measured from the W boson data using the event-averaged response of towers separated in azimuth from the lepton direction.

$\vec{p}$, E calibration - lepton removal

- We remove the calorimeter towers containing lepton energy from the hadronic recoil calculation

 – Lost underlying event energy is measured in φ-rotated windows in W boson data

$$\Delta M_W = 1 \text{ MeV}$$
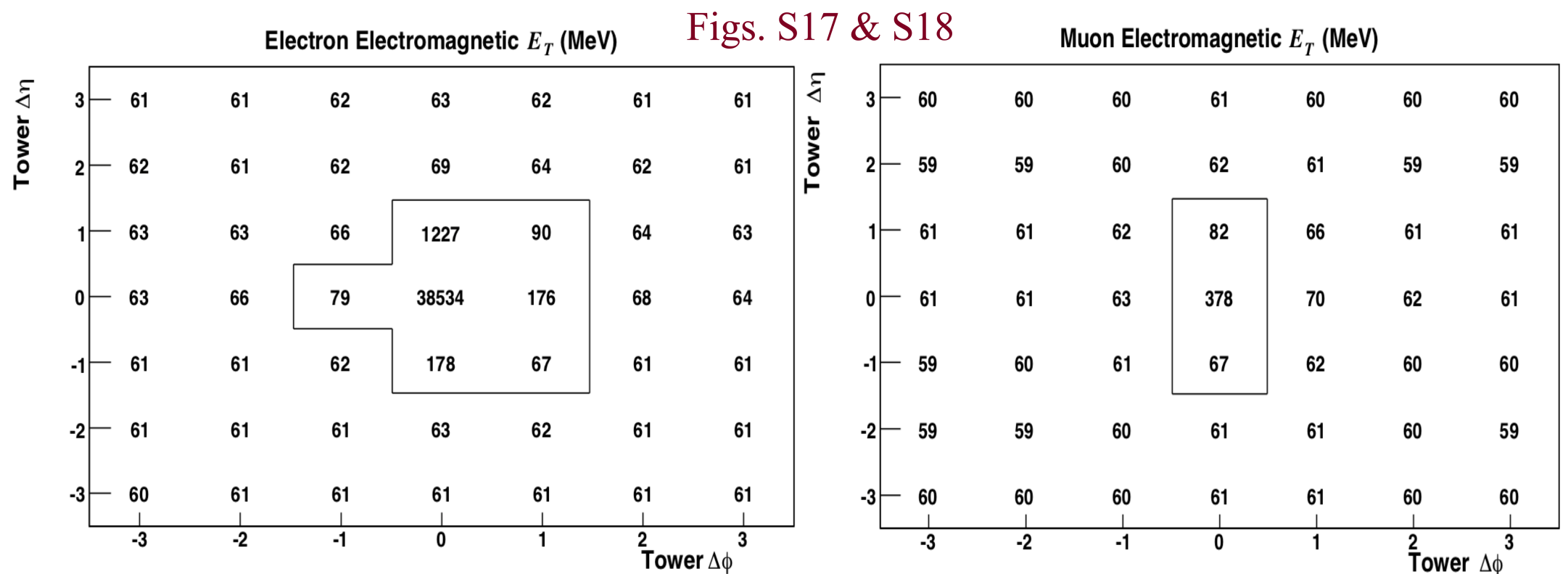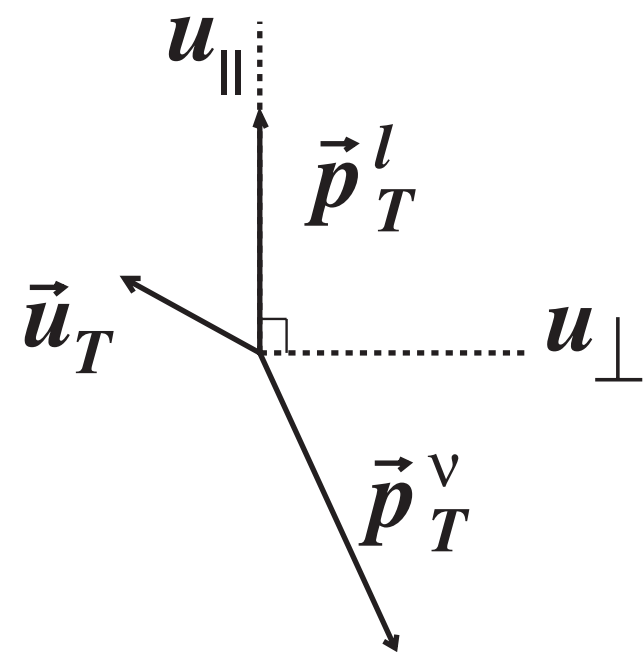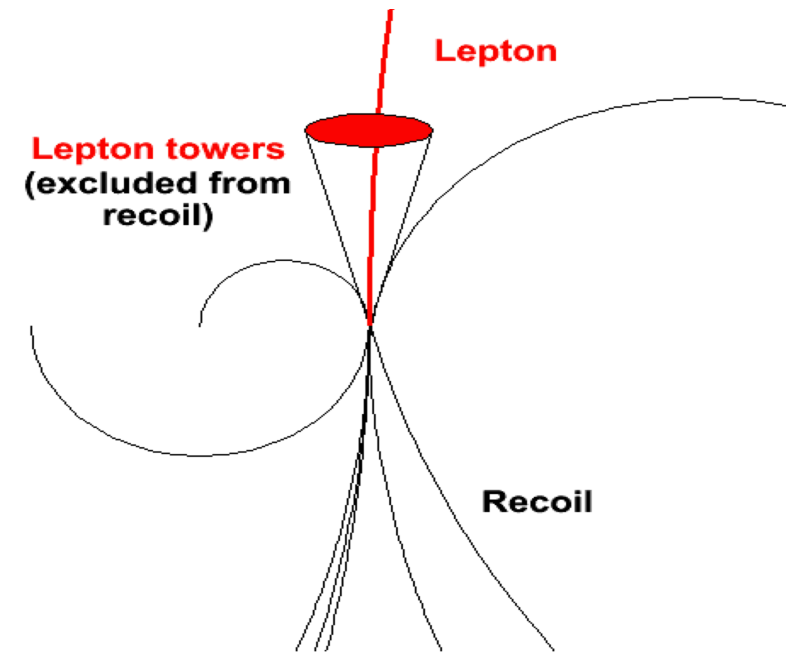
Figs. S17 & S18

Electron Electromagnetic E_T (MeV)

Tower Δη	-3	-2	-1	0	1	2	3
3	61	61	62	63	62	61	61
2	62	61	62	69	64	62	61
1	63	63	66	1227	90	64	63
0	63	66	79	38534	176	68	64
-1	61	61	62	178	67	61	61
-2	61	61	61	63	62	61	61
-3	60	61	61	61	61	61	61

Tower Δφ

Muon Electromagnetic E_T (MeV)

Tower Δη	-3	-2	-1	0	1	2	3
3	60	60	60	61	60	60	60
2	59	59	60	62	61	59	59
1	61	61	62	82	66	61	61
0	61	61	63	378	70	62	61
-1	59	60	61	67	62	60	60
-2	59	59	60	61	61	60	59
-3	60	60	60	61	61	60	60

Tower Δφ

A. V. Kotwal, SLAC, 4/11/22

57

$\overrightarrow{p}$, E **calibration** - **lepton removal**

ings, reproducing the collision environment of the *W* and *Z* boson data. Because there are no $\overrightarrow{p}_T$ events
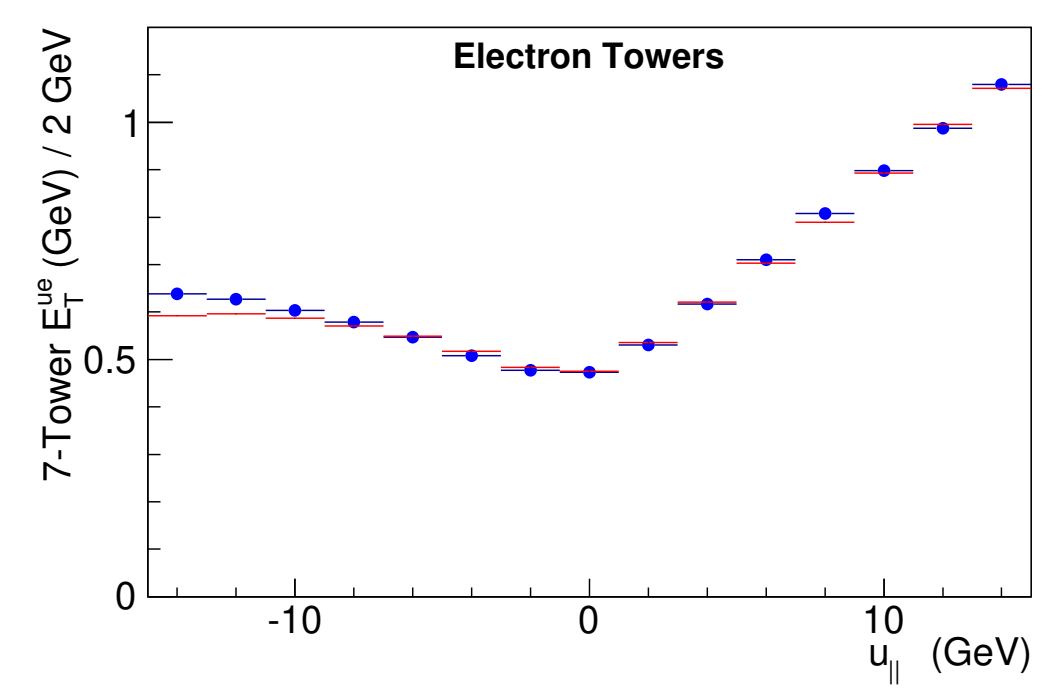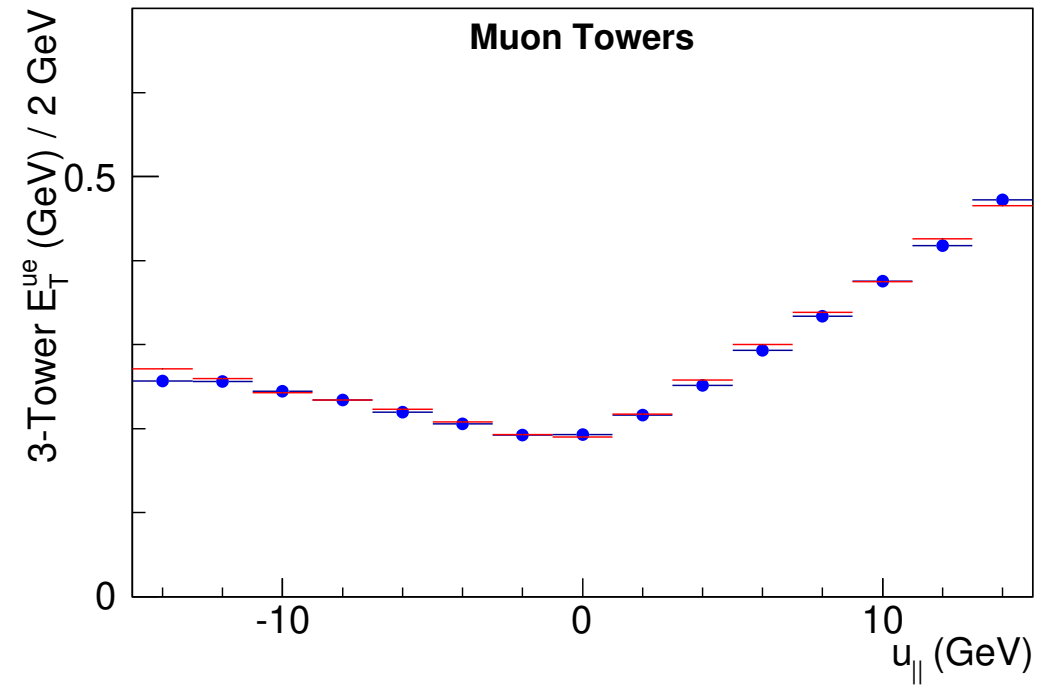
response to, and resolution of, the initial-state QCD radiation accompanying boson production. The simulation of the recoil vector $\overrightarrow{u}$ also requires knowledge of the distribution of the energy flow into the calorimeter towers impacted by the leptons, because these towers are excluded from the computation of $\overrightarrow{u}$. This energy flow is measured from the *W* boson data using the event-averaged response of towers separated in azimuth from the lepton direction.
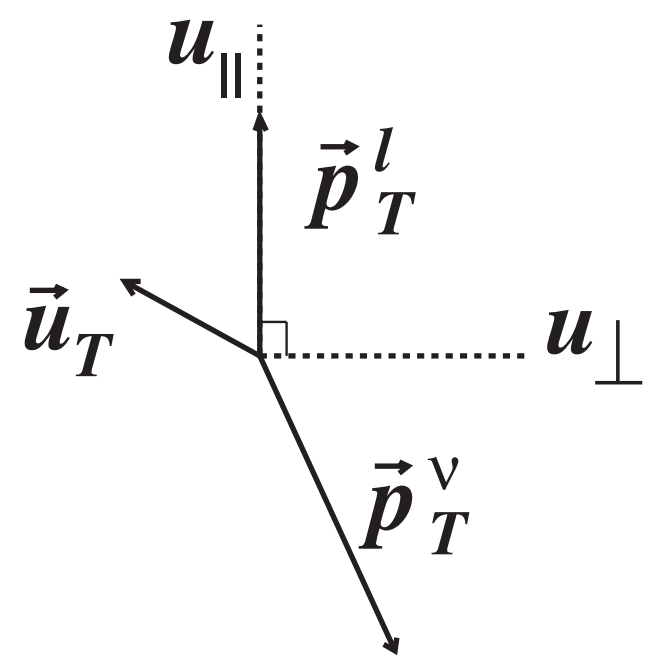
Fraction of zero hadronic energy in the region of removal
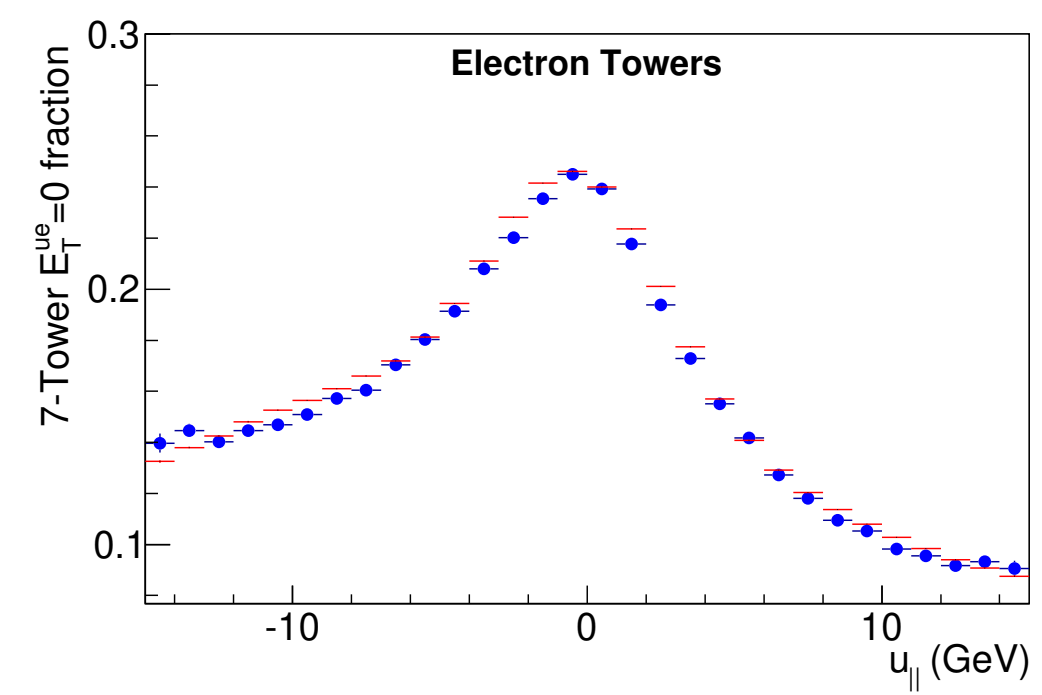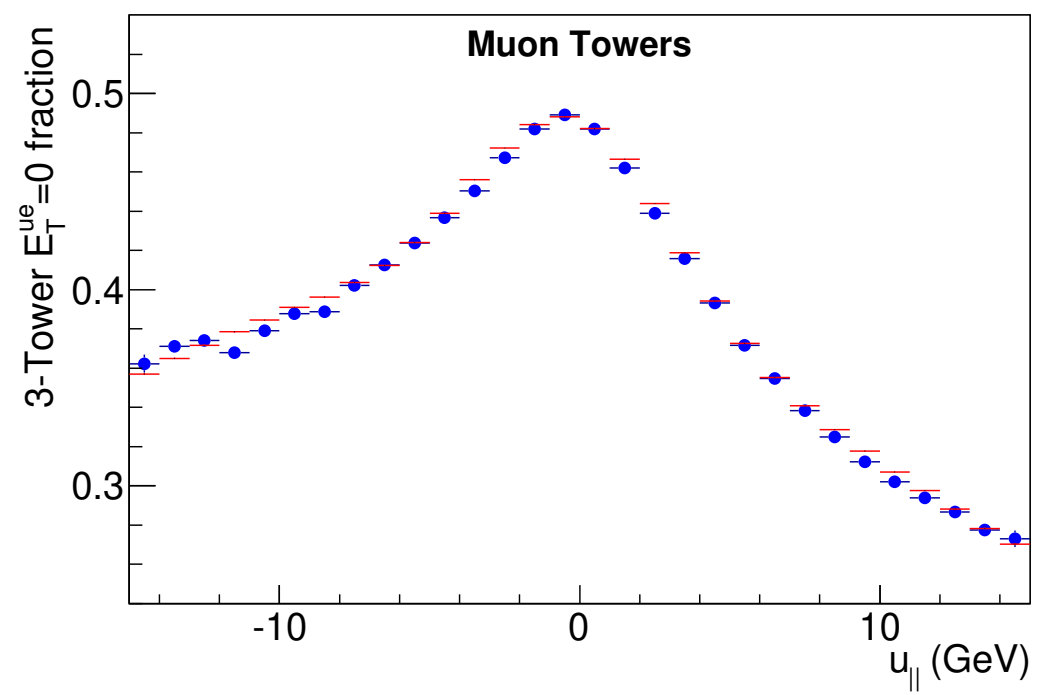
Hadronic E_T in the removal region

Extracting the W boson mass

Kinematic distributions of background events passing the event selection are included in the template fits with their estimated normalizations. The W boson samples contain a small contamination of background events arising from QCD jet production with a hadron misidentified as a lepton, $Z \to \ell\ell$ decays with only one reconstructed lepton, $W \to \tau\nu \to \ell\nu\bar{\nu}\nu$, pion and kaon decays in flight to muons (DIF), and cosmic-ray muons (τ, tau lepton; $\bar{\nu}$, antineutrino). The jet, DIF, and cosmic-ray backgrounds are estimated from control samples of data, whereas the $Z \to \ell\ell$ and $W \to \tau\nu$ backgrounds are estimated from simulation. Background fractions for the muon (electron) datasets are evaluated to be 7.37% (0.14%) from $Z \to \ell\ell$ decays, 0.88% (0.94%) from $W \to \tau\nu$ decays, 0.01% (0.34%) from jets, 0.20% from DIF, and 0.01% from cosmic rays.

The fit results (Fig. 4) are summarized in Table 1. The M_W fit values are blinded during analysis with an unknown additive offset in the range of −50 to 50 MeV, in the same manner as, but independent of, the value used for blinding the Z boson mass fits. As the fits to the different kinematic variables have different sensitivities to systematic uncertainties, their consistency confirms that the sources of systematic uncertainties are well understood. Systematic uncertainties, propagated by varying the simulation parameters within their uncertainties and repeating the fits to these simulated data, are shown in Table 1. The correlated uncertainty in the m_T (p_T^ℓ, p_T^ν) fit between the muon and electron channels is 5.8 (7.9, 7.4) MeV. The mass fits are stable with respect to variations of the fitting ranges.
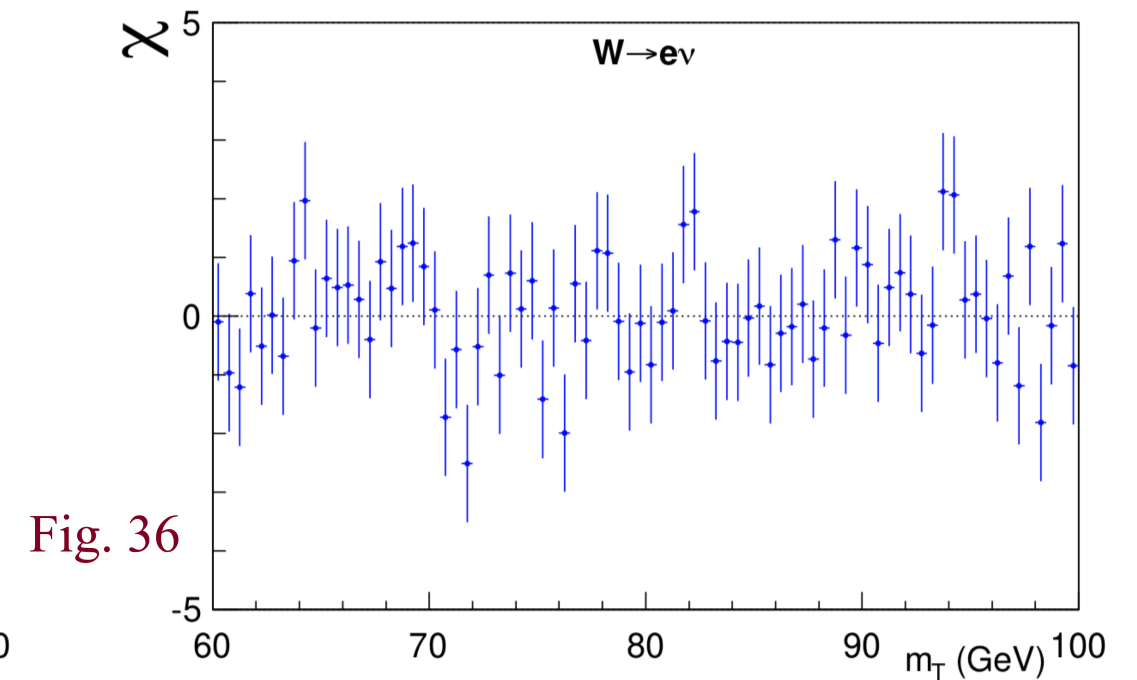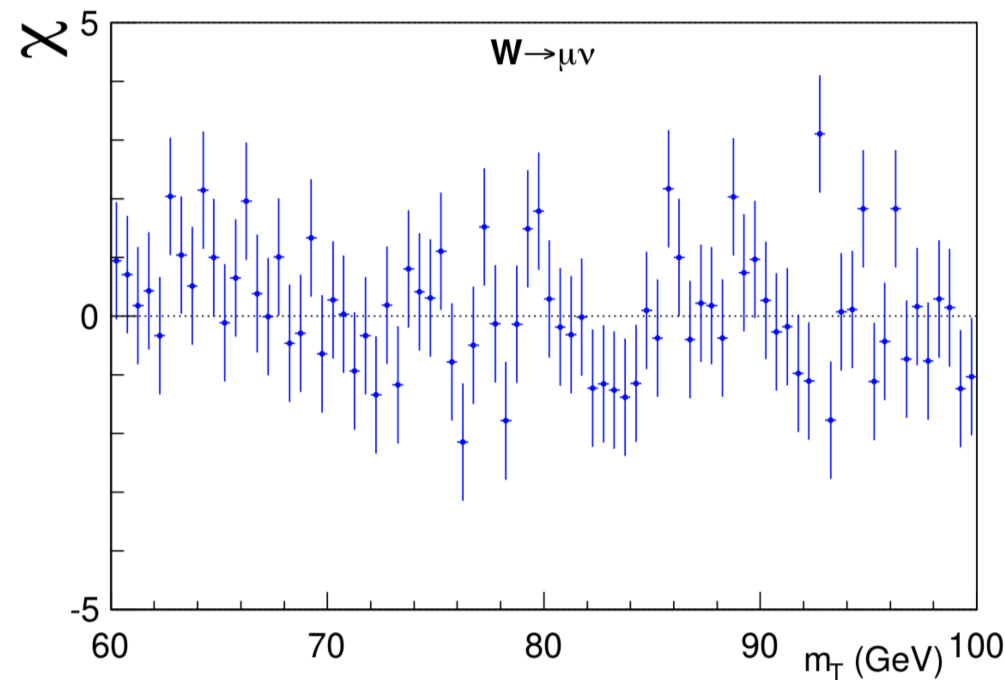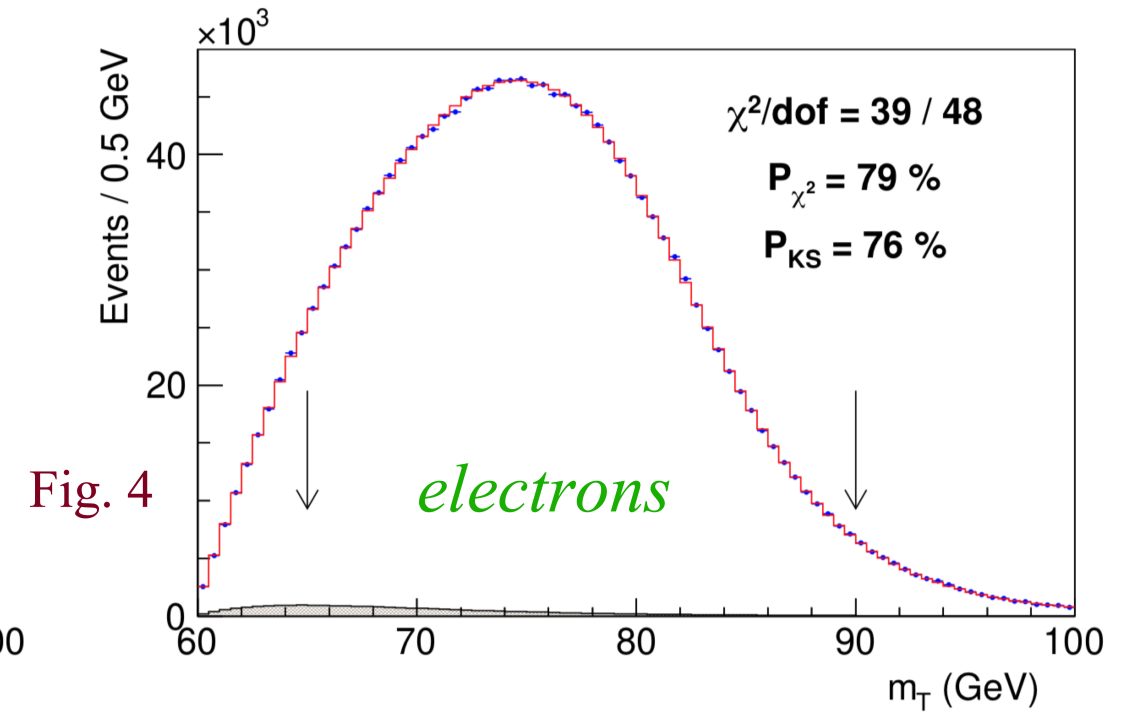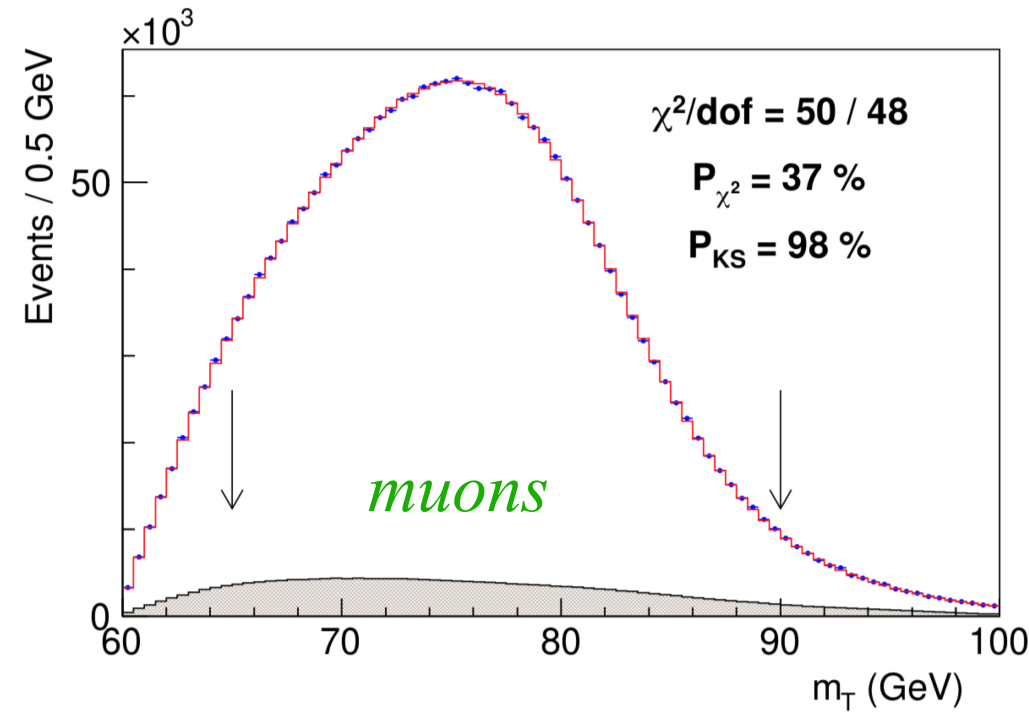
Simulated experiments are used to evaluate the statistical correlations between fits, which are found to be 69% (68%) between m_T and p_T^ℓ (p_T^ν) fit results and 28% between p_T^ℓ and p_T^ν fit results (43). The six individual M_W results are combined (including correlations) by means of the best linear unbiased estimator (66) to obtain $M_W = 80{,}433.5 \pm 9.4$ MeV, with χ^2/dof = 7.4/5 corresponding to a probability of 20%. The m_T, p_T^ℓ, and p_T^ν fits in the electron (muon) channel contribute weights of 30.0% (34.2%), 6.7% (18.7%), and 0.9% (9.5%), respectively. The combined result is shown in Fig. 1, and its associated systematic uncertainties are shown in Table 2.

m_W **extraction**

and cosmic-ray muons (τ, tau lepton; $\bar{\nu}$, anti-neutrino). The jet, DIF, and cosmic-ray backgrounds are estimated from control samples of data, whereas the $Z \to \ell\ell$ and $W \to \tau\nu$ backgrounds are estimated from simulation. Background fractions for the muon (electron) datasets are evaluated to be 7.37% (0.14%) from $Z \to \ell\ell$ decays, 0.88% (0.94%) from $W \to \tau\nu$ decays, 0.01% (0.34%) from jets, 0.20% from DIF, and 0.01% from cosmic rays.

The fit results (Fig. 4) are summarized in Table 1. The M_W fit values are blinded during analysis with an unknown additive offset in the range of −50 to 50 MeV, in the same manner as, but independent of, the value used for blinding the Z boson mass fits. As the fits to the different kinematic variables have different sensitivities to systematic uncertainties, their consistency confirms that the sources of systematic uncertainties are well understood. Systematic uncertainties, propagated by varying the simulation parameters within their uncertainties and repeating the fits to these simulated data, are shown in Table 1. The correlated uncertainty in the m_{T} (p_{T}^{ℓ}, p_{T}^{ν}) fit between the muon and

W Transverse Mass Fits

Fig. 4

Fig. 36

m_W **extraction**

and cosmic-ray muons (τ, tau lepton; $\bar{\nu}$, anti-neutrino). The jet, DIF, and cosmic-ray backgrounds are estimated from control samples of data, whereas the $Z \to \ell\ell$ and $W \to \tau\nu$ backgrounds are estimated from simulation. Background fractions for the muon (electron) datasets are evaluated to be 7.37% (0.14%) from $Z \to \ell\ell$ decays, 0.88% (0.94%) from $W \to \tau\nu$ decays, 0.01% (0.34%) from jets, 0.20% from DIF, and 0.01% from cosmic rays.

The fit results (Fig. 4) are summarized in Table 1. The M_W fit values are blinded during analysis with an unknown additive offset in the range of −50 to 50 MeV, in the same manner as, but independent of, the value used for blinding the Z boson mass fits. As the fits to the different kinematic variables have different sensitivities to systematic uncertainties, their consistency confirms that the sources of systematic uncertainties are well understood. Systematic uncertainties, propagated by varying the simulation parameters within their uncertainties and repeating the fits to these simulated data, are shown in Table 1. The correlated uncertainty in the m_T (p_T^ℓ, p_T^ν) fit between the muon and
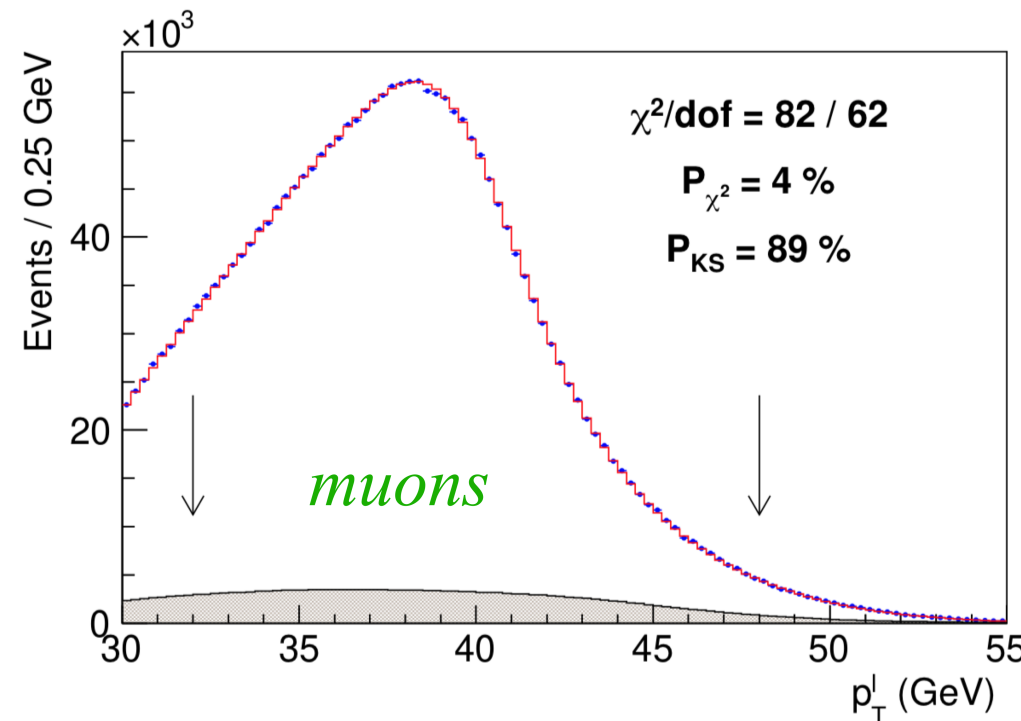
W Charged Lepton p$_T$ Fits

Fig. 4

Fig. 37

m_W extraction

and cosmic-ray muons (τ, tau lepton; $\bar{\nu}$, anti-neutrino). The jet, DIF, and cosmic-ray backgrounds are estimated from control samples of data, whereas the $Z \to \ell\ell$ and $W \to \tau\nu$ backgrounds are estimated from simulation. Background fractions for the muon (electron) datasets are evaluated to be 7.37% (0.14%) from $Z \to \ell\ell$ decays, 0.88% (0.94%) from $W \to \tau\nu$ decays, 0.01% (0.34%) from jets, 0.20% from DIF, and 0.01% from cosmic rays.

The fit results (Fig. 4) are summarized in Table 1. The M_W fit values are blinded during analysis with an unknown additive offset in the range of −50 to 50 MeV, in the same manner as, but independent of, the value used for blinding the Z boson mass fits. As the fits to the different kinematic variables have different sensitivities to systematic uncertainties, their consistency confirms that the sources of systematic uncertainties are well understood. Systematic uncertainties, propagated by varying the simulation parameters within their uncertainties and repeating the fits to these simulated data, are shown in Table 1. The correlated uncertainty in the m_T (p_T^ℓ, p_T^ν) fit between the muon and

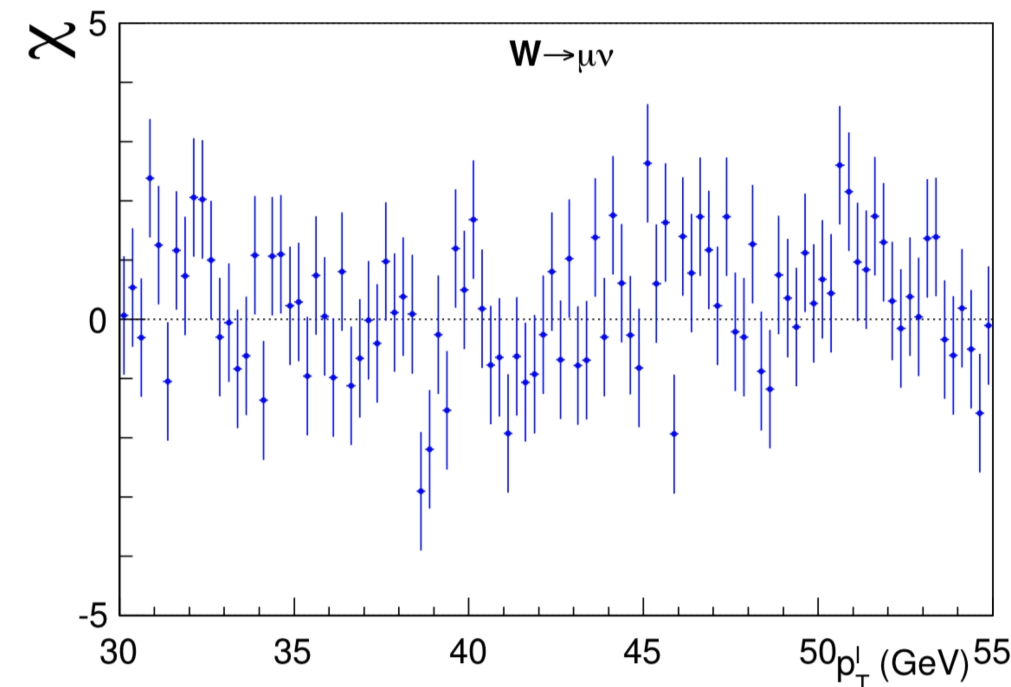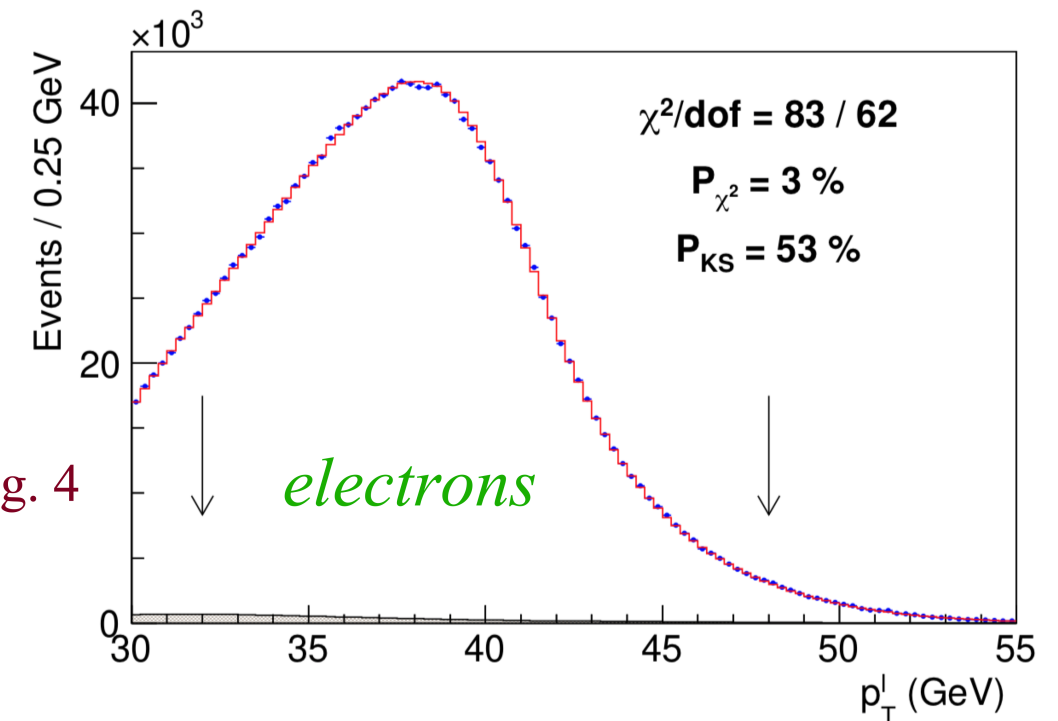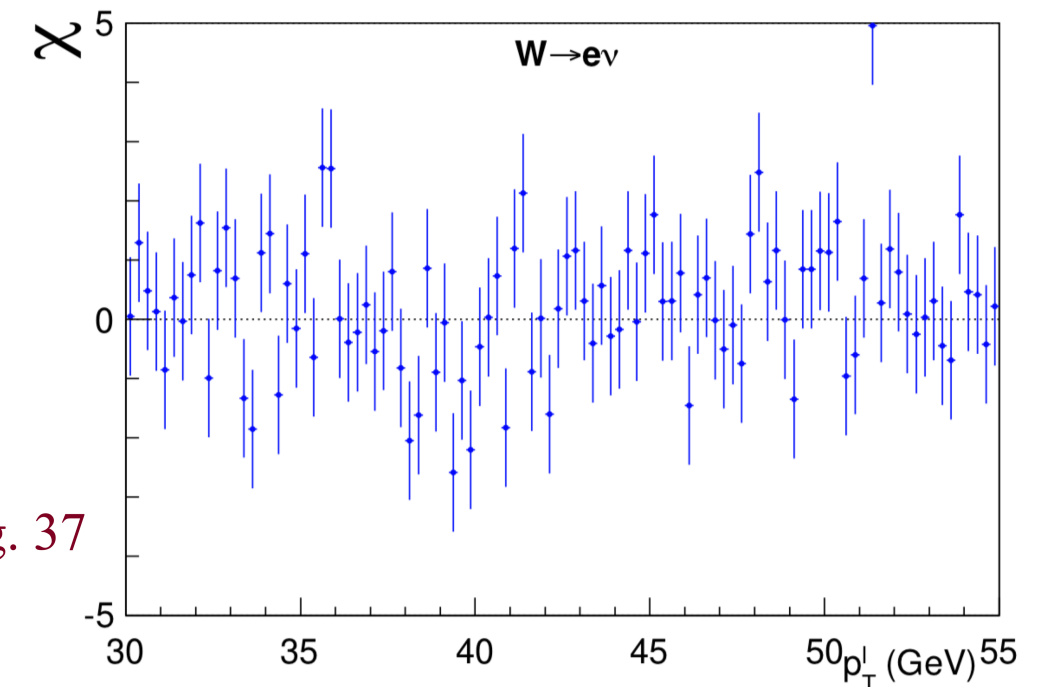## W Neutrino p_T Fits
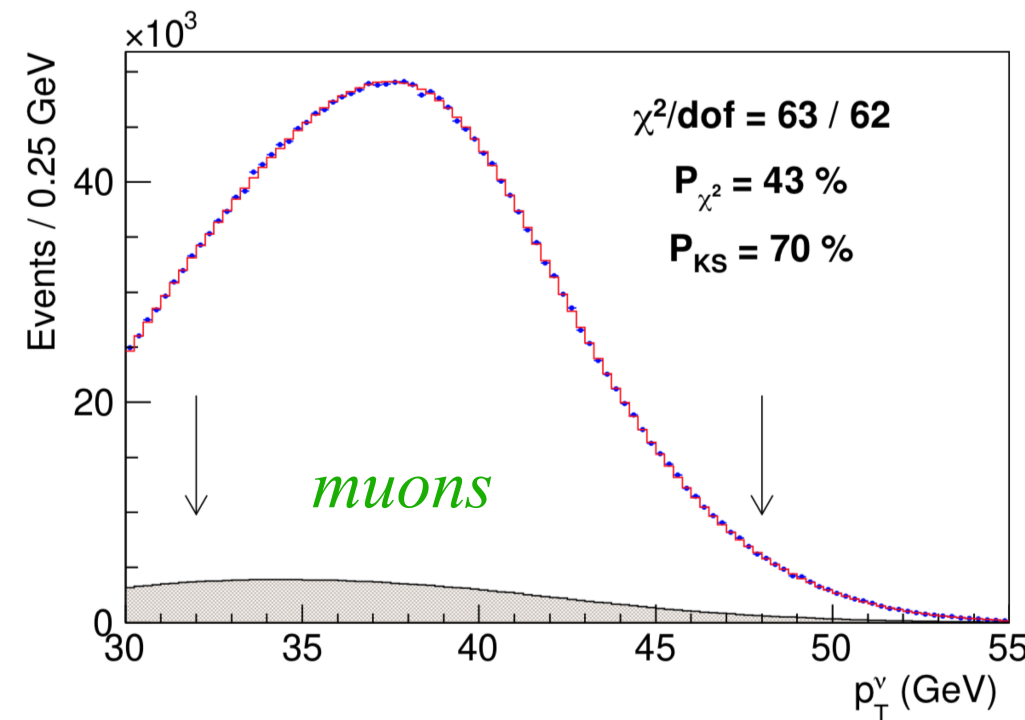
Fig. 4

Fig. 38

m_W **extraction**

and cosmic-ray muons (τ, tau lepton; $\bar{\nu}$, antineutrino). The jet, DIF, and cosmic-ray backgrounds are estimated from control samples of data, whereas the $Z \rightarrow \ell\ell$ and $W \rightarrow \tau\nu$ backgrounds are estimated from simulation. Background fractions for the muon (electron) datasets are evaluated to be 7.37% (0.14%) from $Z \rightarrow \ell\ell$ decays, 0.88% (0.94%) from $W \rightarrow \tau\nu$ decays, 0.01% (0.34%) from jets, 0.20% from DIF, and 0.01% from cosmic rays.

The fit results (Fig. 4) are summarized in Table 1. The M_W fit values are blinded during analysis with an unknown additive offset in the range of –50 to 50 MeV, in the same manner as, but independent of, the value used for blinding the Z boson mass fits. As the fits to the different kinematic variables have different sensitivities to systematic uncertainties, their consistency confirms that the sources of systematic uncertainties are well understood. Systematic uncertainties, propagated by varying the simulation parameters within their uncertainties and repeating the fits to these simulated data, are shown in Table 1. The correlated uncertainty in the m_T (p_T^ℓ, p_T^ν) fit between the muon and
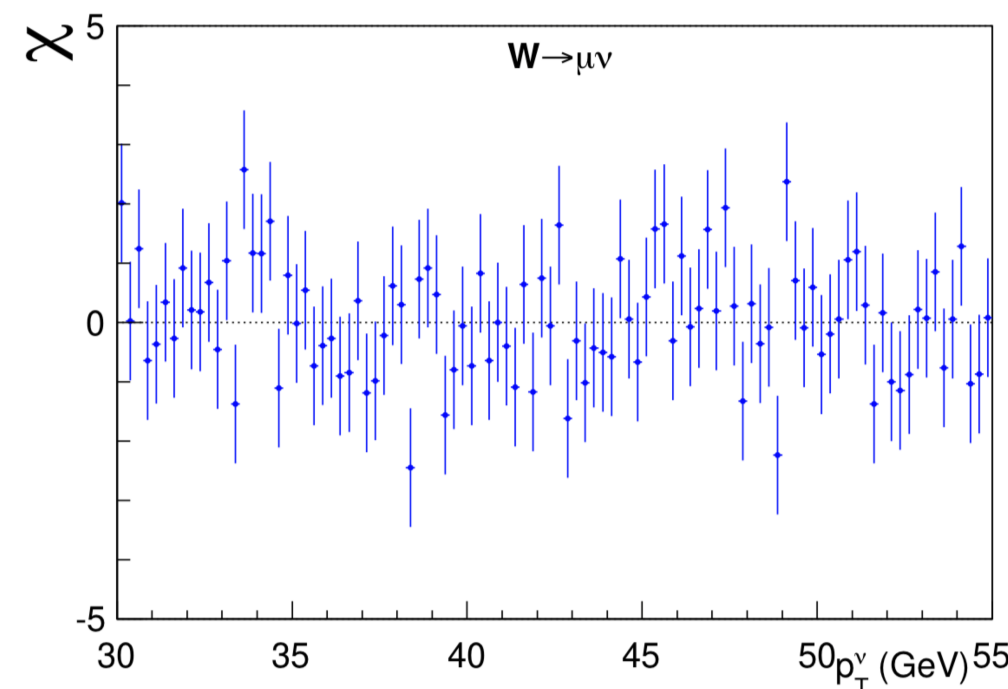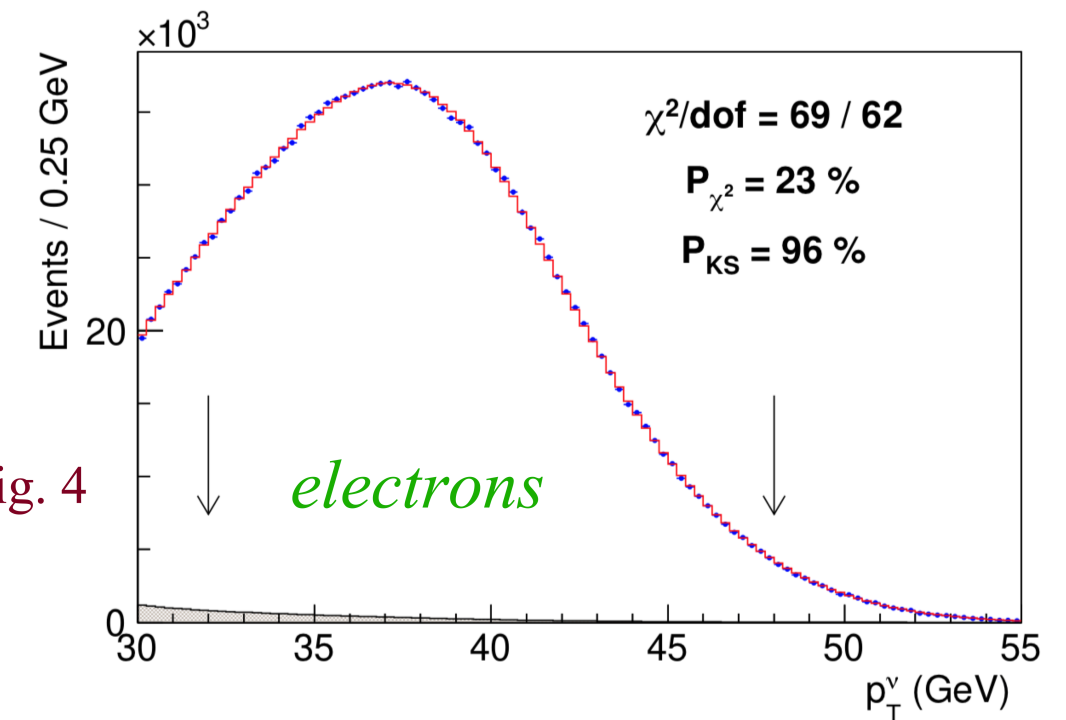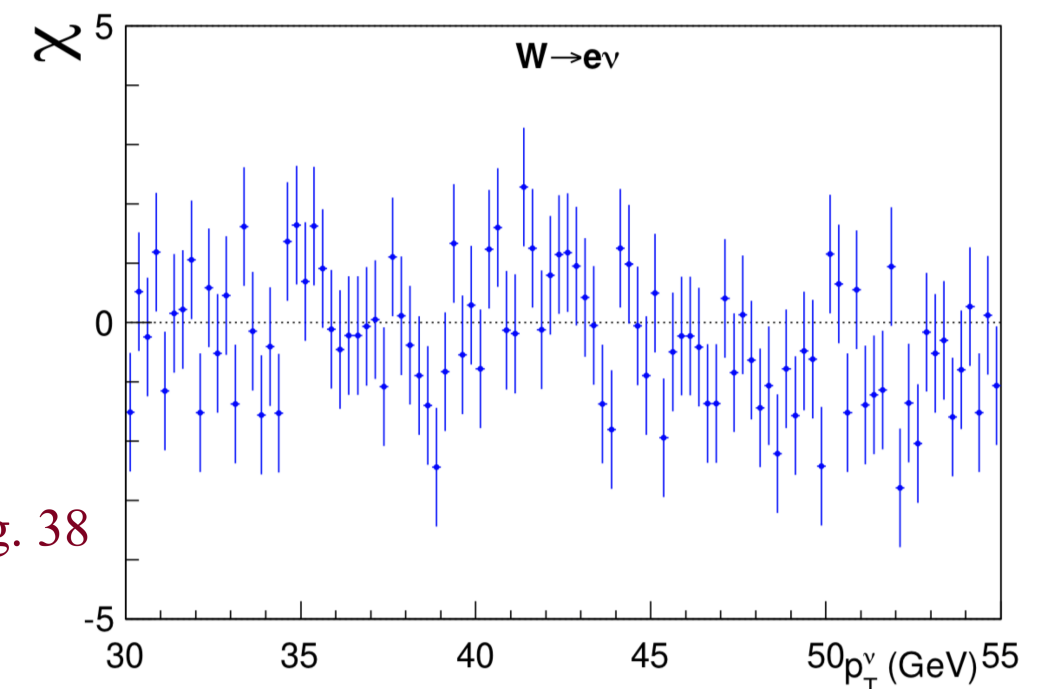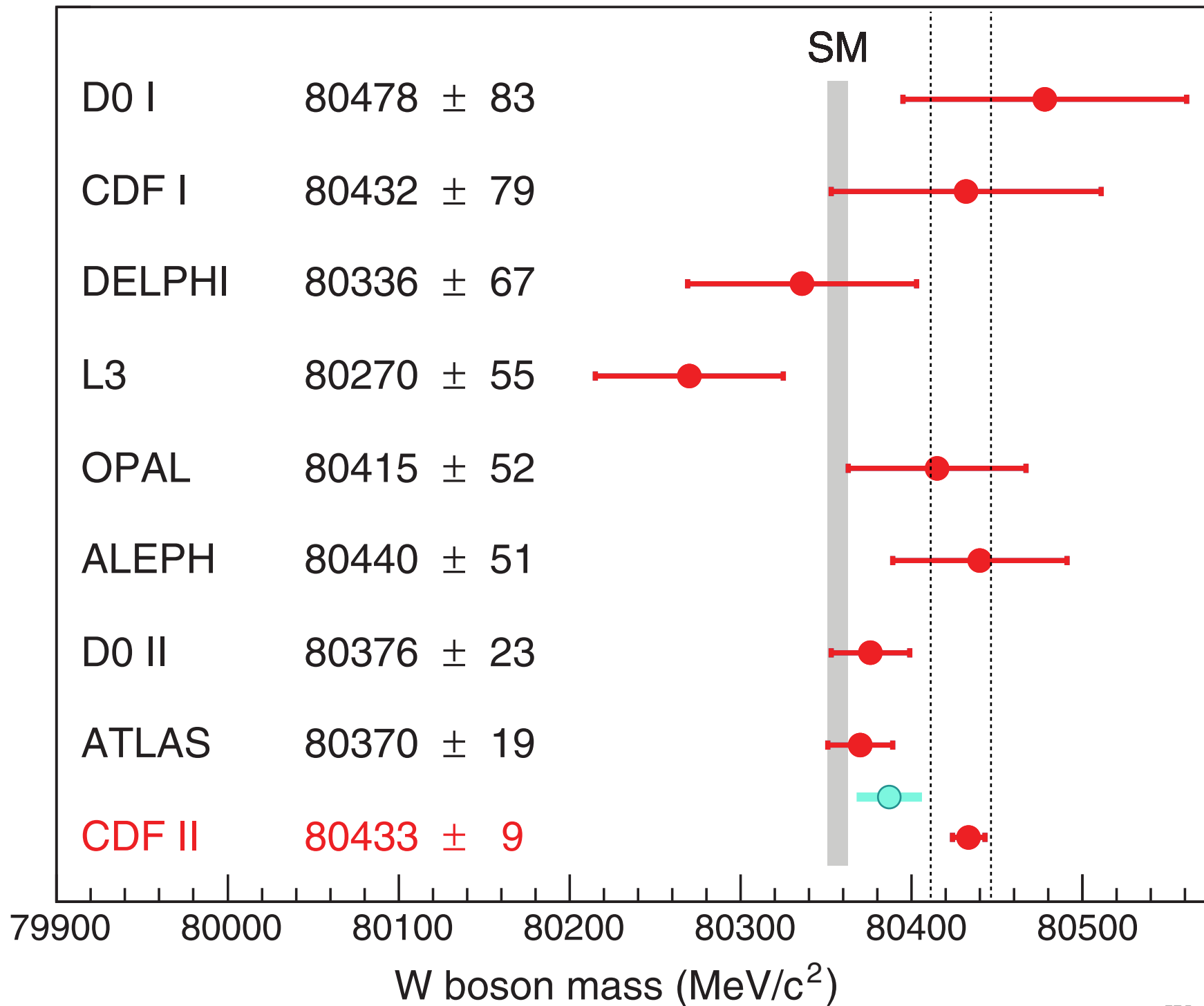
Table 1. Individual fit results and uncertainties for the M_W measurements. The fit ranges are 65 to 90 GeV for the m_T fit and 32 to 48 GeV for the p_T^ℓ and p_T^ν fits. The χ^2 of the fit is computed from the expected statistical uncertainties on the data points. The bottom row shows the combination of the six fit results by means of the best linear unbiased estimator (66).

Distribution	W boson mass (MeV)	χ^2/dof
$m_T(e, \nu)$	$80{,}429.1 \pm 10.3_{\text{stat}} \pm 8.5_{\text{syst}}$	39/48
$p_T^\ell(e)$	$80{,}411.4 \pm 10.7_{\text{stat}} \pm 11.8_{\text{syst}}$	83/62
$p_T^\nu(e)$	$80{,}426.3 \pm 14.5_{\text{stat}} \pm 11.7_{\text{syst}}$	69/62
$m_T(\mu, \nu)$	$80{,}446.1 \pm 9.2_{\text{stat}} \pm 7.3_{\text{syst}}$	50/48
$p_T^\ell(\mu)$	$80{,}428.2 \pm 9.6_{\text{stat}} \pm 10.3_{\text{syst}}$	82/62
$p_T^\nu(\mu)$	$80{,}428.9 \pm 13.1_{\text{stat}} \pm 10.9_{\text{syst}}$	63/62
Combination	$80{,}433.5 \pm 6.4_{\text{stat}} \pm 6.9_{\text{syst}}$	7.4/5

m_W **extraction**

D0 I 80478 ± 83

CDF I 80432 ± 79

DELPHI 80336 ± 67

L3 80270 ± 55

OPAL 80415 ± 52

ALEPH 80440 ± 51

D0 II 80376 ± 23

ATLAS 80370 ± 19

CDF II 80433 ± 9

SM

W boson mass (MeV/c^2): 79900, 80000, 80100, 80200, 80300, 80400, 80500

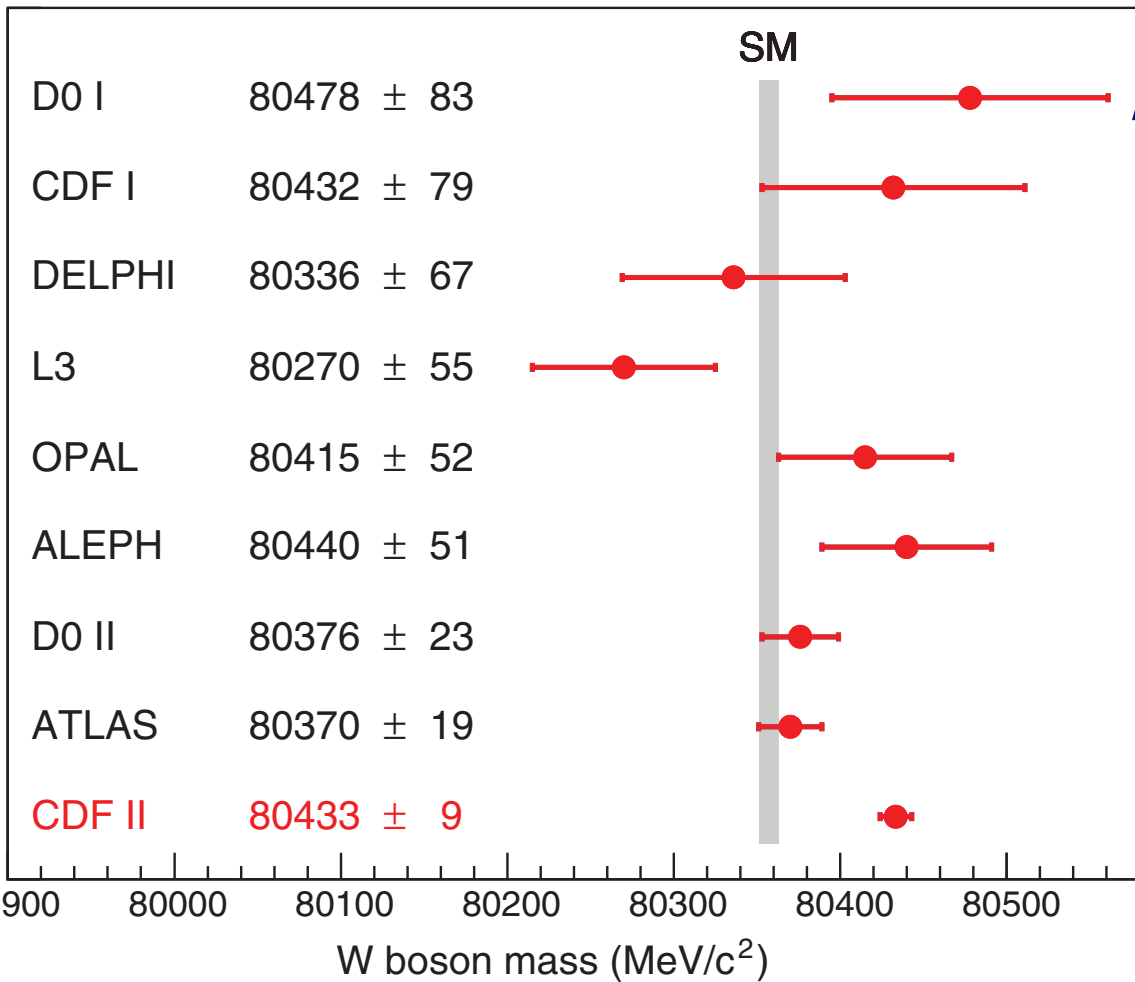W boson mass (MeV/c^2)

⊢○⊣ CDF II (previous) PRD 2014

Table 1. Individual fit results and uncertainties for the M_W measurements. The fit ranges are 65 to 90 GeV for the m_T fit and 32 to 48 GeV for the p_T^ℓ and p_T^ν fits. The χ^2 of the fit is computed from the expected statistical uncertainties on the data points. The bottom row shows the combination of the six fit results by means of the best linear unbiased estimator (66).

Distribution	W boson mass (MeV)	χ^2/dof
$m_T(e, \nu)$	$80{,}429.1 \pm 10.3_{stat} \pm 8.5_{syst}$	39/48
$p_T^\ell(e)$	$80{,}411.4 \pm 10.7_{stat} \pm 11.8_{syst}$	83/62
$p_T^\nu(e)$	$80{,}426.3 \pm 14.5_{stat} \pm 11.7_{syst}$	69/62
$m_T(\mu, \nu)$	$80{,}446.1 \pm 9.2_{stat} \pm 7.3_{syst}$	50/48
$p_T^\ell(\mu)$	$80{,}428.2 \pm 9.6_{stat} \pm 10.3_{syst}$	82/62
$p_T^\nu(\mu)$	$80{,}428.9 \pm 13.1_{stat} \pm 10.9_{syst}$	63/62
Combination	$80{,}433.5 \pm 6.4_{stat} \pm 6.9_{syst}$	7.4/5

We present a measurement of the W-boson mass, M_W, using data corresponding to 2.2 fb^{-1} of integrated luminosity collected in $p\bar{p}$ collisions at $\sqrt{s} = 1.96$ TeV with the CDF II detector at the Fermilab Tevatron. The selected sample of 470 126 $W \rightarrow e\nu$ candidates and 624 708 $W \rightarrow \mu\nu$ candidates yields the measurement $M_W = 80387 \pm 12(\text{stat}) \pm 15(\text{syst}) = 80387 \pm 19$ MeV/c^2. This is the most precise single measurement of the W-boson mass to date.

m_W **extraction**

		SM
D0 I	80478 ± 83	
CDF I	80432 ± 79	
DELPHI	80336 ± 67	
L3	80270 ± 55	
OPAL	80415 ± 52	
ALEPH	80440 ± 51	
D0 II	80376 ± 23	
ATLAS	80370 ± 19	
CDF II	80433 ± 9	

W boson mass (MeV/c^2)

electron channels is 5.8 (7.9, 7.4) MeV. The mass fits are stable with respect to variations of the fitting ranges.

Simulated experiments are used to evaluate the statistical correlations between fits, which are found to be 69% (68%) between m_T and p_T^ℓ (p_T^ν) fit results and 28% between p_T^ℓ and p_T^ν fit results (*43*). The six individual M_W results are combined (including correlations) by means of the best linear unbiased estimator (*66*) to obtain $M_W = 80{,}433.5 \pm 9.4\,\text{MeV}$, with $\chi^2/\text{dof} = 7.4/5$ corresponding to a probability of 20%. The m_T, p_T^ℓ, and p_T^ν fits in the electron (muon) channel contribute weights of 30.0% (34.2%), 6.7% (18.7%), and 0.9% (9.5%), respectively. The combined result is shown in Fig. 1, and its associated systematic uncertainties are shown in Table 2.

analysis with an unknown additive offset in the range of −50 to 50 MeV, in the same manner as, but independent of, the value used for blinding the Z boson mass fits. As the fits to the different kinematic variables have different sensitivities to systematic uncertainties, their consistency confirms that the sources of systematic uncertainties are well understood. Systematic uncertainties, propagated by varying the simulation parameters within their uncertainties and repeating the fits to these simulated data, are shown in Table 1. The correlated uncertainty in the m_T (p_T^ℓ, p_T^ν) fit between the muon and

Table 2. Uncertainties on the combined M_W result.

Source	Uncertainty (MeV)
Lepton energy scale	3.0
Lepton energy resolution	1.2
Recoil energy scale	1.2
Recoil energy resolution	1.8
Lepton efficiency	0.4
Lepton removal	1.2
Backgrounds	3.3
p_T^Z model	1.8
p_T^W/p_T^Z model	1.3
Parton distributions	3.9
QED radiation	2.7
W boson statistics	6.4
Total	9.4

Systematic uncertainties

Previous CDF Result (2.2 fb⁻¹)
Transverse Mass Fit Uncertainties (MeV)

	electrons	muons	common
W statistics	19	16	0
Lepton energy scale	10	7	5
Lepton resolution	4	1	0
Recoil energy scale	5	5	5
Recoil energy resolution	7	7	7
Selection bias	0	0	0
Lepton removal	3	2	2
Backgrounds	4	3	0
pT(W) model	3	3	3
Parton dist. Functions	10	10	10
QED rad. Corrections	4	4	4
Total systematic	18	16	15
Total	26	23	

New CDF Result (8.8 fb⁻¹)
Transverse Mass Fit Uncertainties (MeV)

	electrons	muons	common
W statistics	10.3	9.2	0
Lepton energy scale	5.8	2.1	1.8
Lepton resolution	0.9	0.3	-0.3
Recoil energy scale	1.8	1.8	1.8
Recoil energy resolution	1.8	1.8	1.8
Selection bias	0.5	0.5	0
Lepton removal	1	1.7	0
Backgrounds	2.6	3.9	0
pT(Z) & pT(W) model	1.1	1.1	1.1
Parton dist. Functions	3.9	3.9	3.9
QED rad. Corrections	2.7	2.7	2.7
Total systematic	8.7	7.4	5.8
Total	13.5	11.8	5.8

Systematic uncertainties shown in green: statistics-limited by control data samples

A. V. Kotwal, SLAC, 4/11/22

Discussion

The dataset used in this analysis is about four times as large as the one used in the previous analysis (*41*, *43*). Although the resolution of the hadronic recoil is somewhat degraded in the new data because of the higher instantaneous luminosity, the statistical precision of the measurement from the larger sample is still improved by almost a factor of 2. To achieve a commensurate reduction in systematic uncertainties, a number of analysis improvements have been incorporated, as described in table S1. These improvements are based on using cosmic-ray and collider data in ways not employed previously to improve (i) the COT alignment and drift model and the uniformity of the EM calorimeter response, and (ii) the accuracy and robustness of the detector response and resolution model in the simulation. Additionally, theoretical inputs to the analysis have been updated. Upon incorporating the improved understanding of PDFs and track reconstruction, our previous measurement is increased by 13.5 MeV to 80,400.5 MeV; the consistency of the latter with the new measurement is at the percent probability level.

D0 I	80478 ± 83
CDF I	80432 ± 79
DELPHI	80336 ± 67
L3	80270 ± 55
OPAL	80415 ± 52
ALEPH	80440 ± 51
D0 II	80376 ± 23
ATLAS	80370 ± 19
CDF II	80433 ± 9

W boson mass (MeV/c^2)

CDF II (previous) PRD 2014
CDF II (2014) re-analyzed
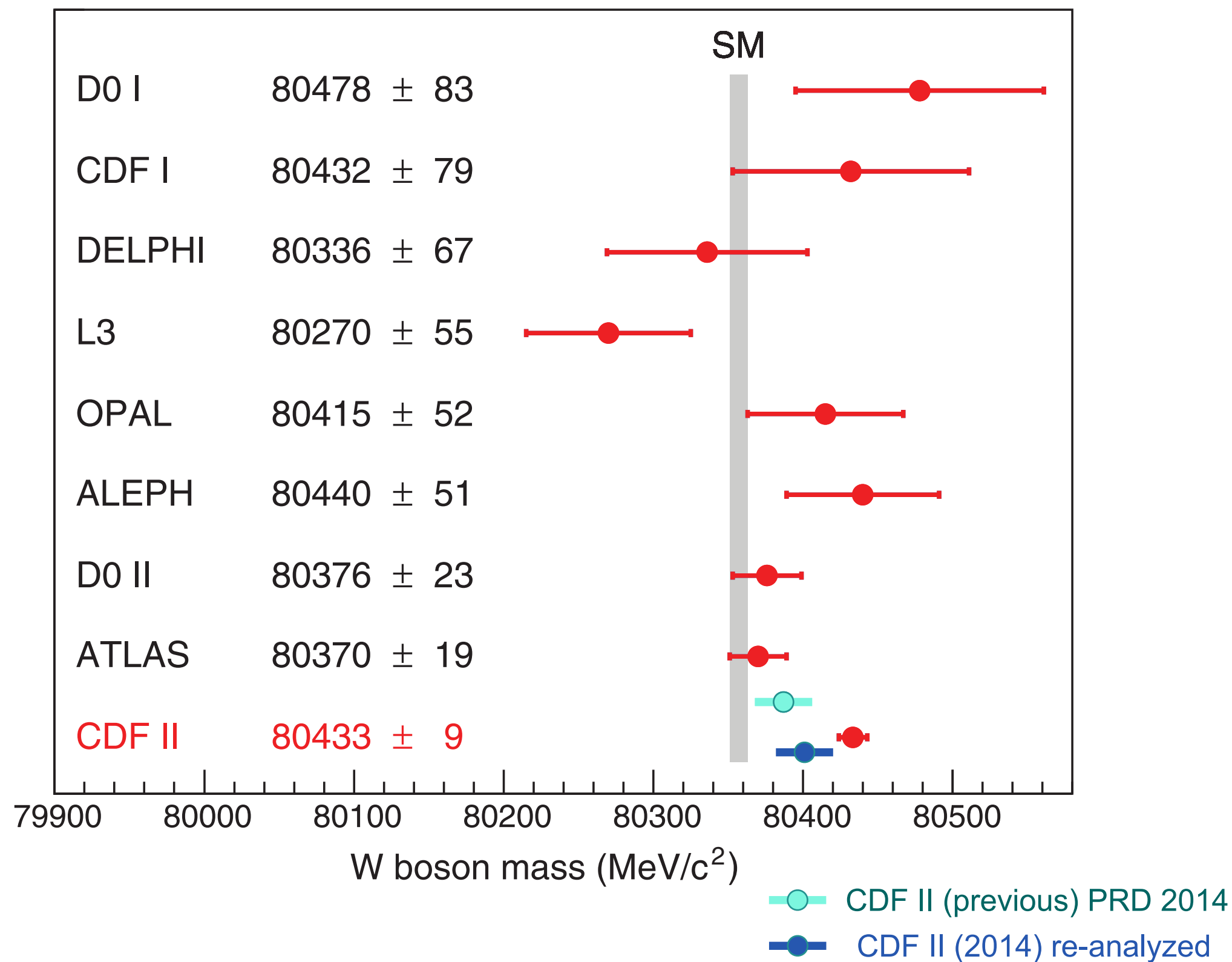
Improvement over previous CDF

Method or technique	impact	section of paper
Detailed treatment of parton distribution functions	+3.5 MeV	IV A
Resolved beam-constraining bias in CDF reconstruction	+10 MeV	VI C
Improved COT alignment and drift model [65]	uniformity	VI
Improved modeling of calorimeter tower resolution	uniformity	III
Temporal uniformity calibration of CEM towers	uniformity	VII A
Lepton removal procedure corrected for luminosity	uniformity	VIII A
Higher-order calculation of QED radiation in J/ψ and Υ decays	accuracy	VI A & B
Modeling kurtosis of hadronic recoil energy resolution	accuracy	VIII B 2
Improved modeling of hadronic recoil angular resolution	accuracy	VIII B 3
Modeling dijet contribution to recoil resolution	accuracy	VIII B 4
Explicit luminosity matching of pileup	accuracy	VIII B 5
Modeling kurtosis of pileup resolution	accuracy	VIII B 5
Theory model of p_T^W/p_T^Z spectrum ratio	accuracy	IV B
Constraint from p_T^W data spectrum	robustness	VIII B 6
Cross-check of p_T^Z tuning	robustness	IV B

Improvement over previous CDF

- The statistical precision of the measurement from the four times larger sample is improved by almost a factor of 2

- To achieve a commensurate reduction in systematic uncertainties, a number of analysis improvements have been incorporated

- These improvements are based on using cosmic-ray and collider data in ways not employed previously to improve

  - ✓ the COT alignment and drift model and the uniformity of the EM calorimeter response

  - ✓ the accuracy and robustness of the detector response and resolution model in the simulation

  - ✓ theoretical inputs to the analysis have been updated

- Upon incorporating the improved understanding of PDFs and track reconstruction, our previous measurement is increased by 13.5 MeV to 80,400.5 MeV

  - ✓ consistency of the latter with the new measurement is at the percent probability level

Conclusion

In conclusion, we report a new measurement of the W boson mass with the complete dataset collected by the CDF II detector at the Fermilab Tevatron, corresponding to 8.8 fb^{-1} of integrated luminosity. This measurement, $M_W = 80,433.5 \pm 9.4$ MeV, is more precise than all previous measurements of M_W combined and subsumes all previous CDF measurements from 1.96-TeV data (*38, 39, 41, 43*). A comparison with the SM expectation of $M_W = 80,357 \pm 6$ MeV (*10*), treating the quoted uncertainties as independent, yields a difference with a significance of 7.0σ and suggests the possibility of improvements to the SM calculation or of extensions to the SM. This comparison, along with past measurements, is shown in Fig. 5. Using the method described in (*45*), we obtain a combined Tevatron (CDF and D0) result of $M_W = 80,427.4 \pm 8.9$ MeV. Assuming no correlation between the Tevatron and LEP measurements, their average becomes $M_W = 80,424.2 \pm 8.7$ MeV.
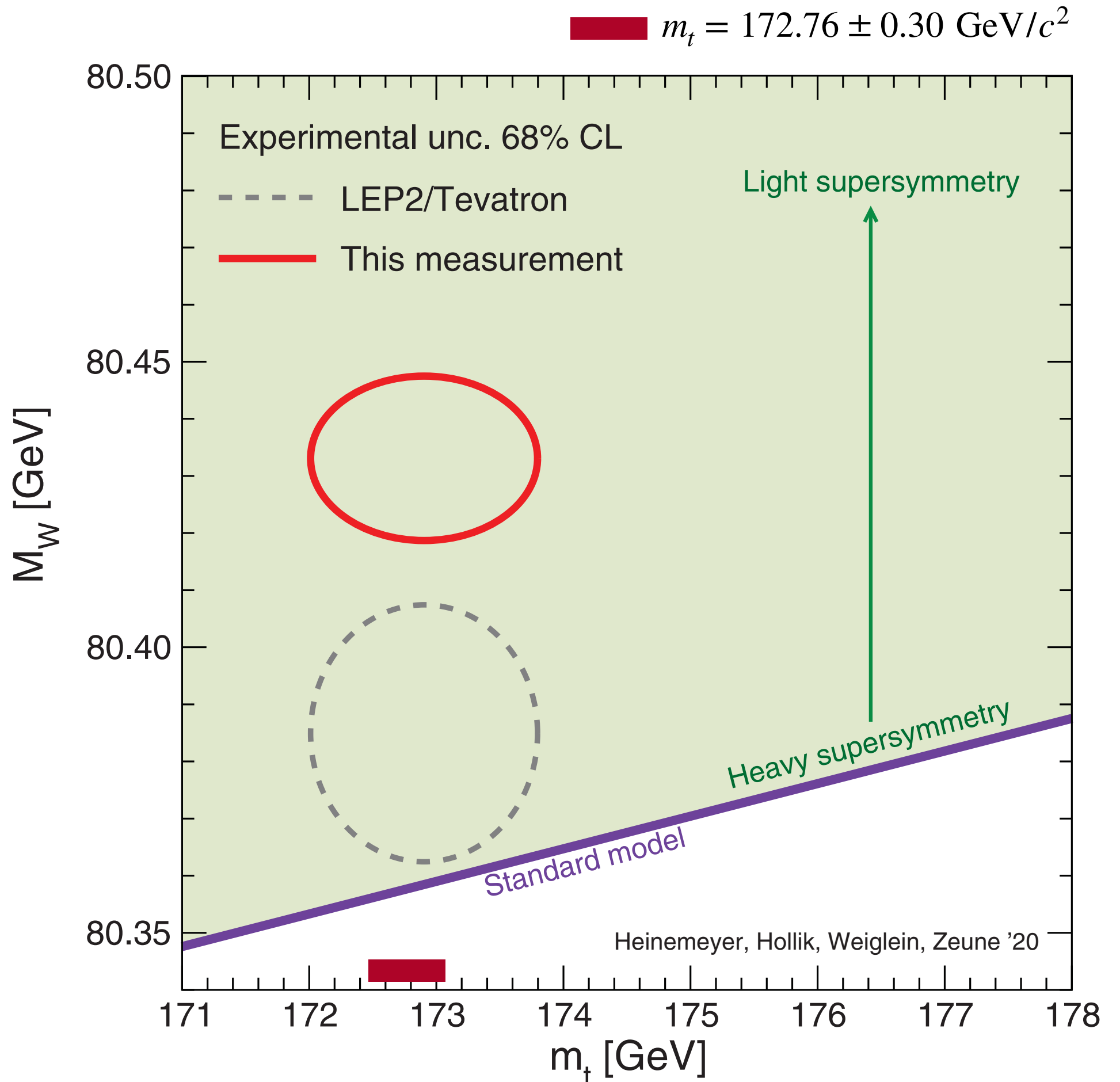
Appendix

from back-up slides of Kotwal seminar

Updates to 2012 Result (2.2 fb^{-1})

- Shift from CTEQ6 to NNPDF3.1 PDF used for central value = +3.5 MeV

- In the 2.2 fb^{-1} analysis, an additional systematic uncertainty was quoted to cover an inconsistency between the NBC and BC Y → μμ mass fits.

- In this analysis we resolve the inconsistency caused by the beam-constraining procedure, eliminating the additional systematic uncertainty and increasing the measured M$_{W}$ value by ≈ 10 MeV.

- The beam-constraining procedure in the CDF track reconstruction software extrapolates the tracks found in the COT inward to the transverse position of the beamline. This extrapolation can and should take into account the energy loss in the material inside the inner radius of the COT (the beampipe, the silicon vertex detector and its services) to infer and update the track parameters at the beam position before applying the beam constraint.

- This update had been deactivated in the reconstruction software used for the previous analysis. By activating this updating feature of the extrapolator, the flaw in the BC Y → μμ mass is corrected, which changes the momentum scale derived from it.

Q & A

Q: Measurement of the W boson mass as a function of running period.

A: Historically, the analysis has been designed as an inclusive analysis. In its current form, measuring the W mass for subsamples of the data requires repeating almost the entire data analysis for each subsample.

For this analysis we invested two years in completely redoing the alignment of the COT, making substantial improvements in both the procedures and the alignment quality metrics, and including dependence on running period (NIM A 762, (2014)).

Compared to the previous analysis, we also invested in improving the uniformity and stability of the EM calorimeter by performing an E/p-based calibration for individual φ-wedges as a function of running period.

However, many aspects of the analysis, including all calibrations related to the hadronic calorimeter and all the backgrounds, cannot yet be performed for subsamples of the data, other than by brute-force repetition. The latter would be a tedious and multi-year process. We plan on improving the functionality of the analysis to handle subsamples, which also improves our understanding of the fundamentals.